Physica D 493 (2026) 135232

Contents lists available at ScienceDirect

Physica D

journal homepage: www.elsevier.com/locate/physd

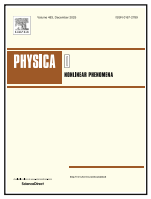

Emergent spatiotemporal dynamics in large-scale brain networks with next generation neural mass models

Rosa Maria Delicado-Moll[a,*], Gemma Huguet[b,c,d], Pau Clusella[b]

[a] Departament de Matemàtiques i Informàtica and Institute of Applied Computing and Community Code (IAC3), Universitat de les Illes Balears, Palma, Spain
[b] Departament de Matemàtiques, Universitat Politècnica de Catalunya, Barcelona, Spain
[c] Institut de Matemàtiques de la UPC - Barcelona Tech (IMTech), Barcelona, Spain
[d] Centre de Recerca Matemàtica, Barcelona, Spain

ARTICLE INFO

Communicated by Dr R Kuske

Keywords:
Large-scale brain models
Next-generation neural mass models
Homogeneous invariant manifold
Transverse instabilities
Master stability function
Floquet theory
Complex spatiotemporal patterns
Lyapunov exponents
Chaos

ABSTRACT

Understanding the dynamics of large-scale brain models remains a central challenge due to the inherent complexity of these systems. In this work, we explore the emergence of complex spatiotemporal patterns in a large-scale brain model composed of 90 interconnected brain regions coupled through empirically derived anatomical connectivity. An important aspect of our formulation is that the local dynamics of each brain region are described by a next-generation neural mass model, which explicitly captures the macroscopic gamma activity of coupled excitatory and inhibitory neural populations (PING mechanism). We first identify the system's homogeneous states—both resting and oscillatory—and analyze their stability under uniform perturbations. Then, we determine the stability against non-uniform perturbations by obtaining dispersion relations for the perturbation growth rate. This analysis enables us to link unstable directions of the homogeneous solutions to the emergence of rich spatiotemporal patterns, that we characterize by means of Lyapunov exponents and frequency spectrum analysis. Our results show that, compared to previous studies with classical neural mass models, next-generation neural mass models provide a broader dynamical repertoire, both within homogeneous states and in the heterogeneous regime. Additionally, we identify a key role for anatomical connectivity in cross-frequency coupling, allowing for the emergence of gamma oscillations with amplitude modulated by slower rhythms. These findings suggest that such models are not only more biophysically grounded but also particularly well-suited to capture the full complexity of large-scale brain dynamics. Overall, our study advances the analytical understanding of emerging spatiotemporal patterns in whole-brain models.

1. Introduction

Oscillatory and rhythmic activity is ubiquitous in the brain, spanning a wide range of frequency bands—from slow delta (1–4 Hz) and theta (4–8 Hz) rhythms to faster alpha (8–13 Hz), beta (13–30 Hz), and gamma (30–100 Hz) oscillations [1]. A key challenge in computational neuroscience is to understand how these dynamics emerge and interact across spatial and temporal scales, giving rise to complex spatiotemporal patterns observed in whole brain recordings [2–5]. Neural mass models (NMMs) represent a primary modeling approach, providing low-dimensional descriptions of population-level dynamics by coarse-graining the activity of large ensembles of neurons and synapses. Canonical formulations such as the Wilson-Cowan [6], the Jansen-Rit [7], and the Wendling models (reviewed in [8]) have been especially successful in reproducing and fitting neuroimaging data, notably EEG and MEG, thereby establishing a principled link between microscopic neural mechanisms and macroscopic brain signals.

By coupling several NMMs using network topologies derived from structural connectomics data, one can produce large-scale brain models (also known as whole-brain models) in which single brain regions described by a NMM interact across nodes. Such models have been widely used to investigate both healthy brain function [2,5,9] and a range of pathological conditions, including Parkinson, epilepsy, schizophrenia or Alzheimer's disease [10–14]. However, these models pose significant challenges for mathematical analysis due to their high dimensionality and the presence of features such as noise, heterogeneities, and transmission delays.

In Clusella et al. [15], the authors present a simple framework to account for the emergence of rich dynamical phenomena, including high-dimensional chaos and traveling waves. By assuming normalized total

* Corresponding author.
E-mail addresses: rosa-maria.delicado@uib.cat (R.M. Delicado-Moll), gemma.huguet@upc.edu (G. Huguet), pau.clusella@upc.edu (P. Clusella).

https://doi.org/10.1016/j.physd.2026.135232
Received 1 December 2025; Received in revised form 3 March 2026; Accepted 6 April 2026
Available online 8 April 2026

inputs received by the nodes, they demonstrate that such complex behaviors can arise purely from network coupling. Their analysis builds on the study of transverse instabilities of homogeneous oscillatory solutions: using the Master Stability Function (MSF) formalism [16], they showed how an oscillatory state of identical node dynamics —modeled by the Jansen-Rit system [7]— can lose stability, giving rise to a diverse repertoire of spatiotemporal patterns.

While most large-scale brain models rely on classical neural mass formulations such as Jansen-Rit, recent advances in mean field theory have led to a new generation of neural mass models that provide an exact description of the macroscopic activity of spiking neuronal networks [17,18]. Unlike classical NMMs, the so-called next-generation NMMs (NG-NMMs) capture the exact evolution of the mean firing rate and membrane potential of a population of quadratic integrate-and-fire (QIF) neurons, with dynamics that depend on neuronal synchrony within the population, yielding a richer repertoire of behaviors. Their combination of accuracy and interpretability has drawn significant attention [18–24], and they are now widely used to address diverse questions in neuroscience [25–28]. In particular, incorporating NG-NMM into large-scale brain modeling frameworks represents a promising and rapidly emerging area of research [28–30].

Following this line of research, in the present work we investigate the dynamics of a large-scale brain model consisting of a network of 90 nodes, with structural connectivity derived from tractography data using the AAL90 atlas, a standardized parcellation that divides the brain into 90 regions [31,32]. The activity of each node is governed by a NG-NMM composed of an excitatory and an inhibitory population interacting through exponentially decaying synapses. For this exploration, we adopt parameter values from previous studies [19,27], thereby representing an instance of the Pyramidal-Interneuron Network Gamma (PING) mechanism for generation of gamma oscillations [33–37].

We provide a thorough analysis of the resulting network dynamics, emphasizing how the incorporation of NG-NMMs shapes large-scale brain activity patterns. Following the approach of [15], we highlight that such models are capable of generating rich dynamical phenomena, including traveling waves and high-dimensional chaos, under minimal assumptions. Our analysis begins by identifying a homogeneous manifold of the system (corresponding to identical node dynamics) that serves as a reference structure for understanding the emergence of more complex spatiotemporal behaviors. The dynamics on the manifold are captured by a low-dimensional nonlinear system, which we analyze using numerical continuation methods. We then investigate the stability of homogeneous fixed points and limit cycles to arbitrary perturbations by decomposing them on a suitable basis, ultimately providing a dispersion relation or Master Stability Function that links spatial modes with perturbation growth rates. Simulations and analysis of Lyapunov exponents and frequency spectrum reveal that when this manifold loses stability, it gives rise to a diverse range of dynamical patterns.

Our results show that this large-scale brain model exhibits a broader repertoire of dynamical behaviors than those reported in Clusella et al. [15], both within the homogeneous manifold and in the heterogeneous regime. Indeed, we find instabilities arising from both stationary and oscillatory states. Among the relevant patterns observed, we highlight the presence of fast oscillations whose amplitude is modulated by a slower rhythm—a pattern that cannot be generated in the isolated nodes. This phenomenon is a type of cross-frequency coupling (CFC) [37] widely observed in the brain, particularly in the hippocampus, where theta-gamma coupling structures neural firing into temporally ordered assemblies believed to underlie memory formation and spatial coding [38]. Our results suggest that NG-NMMs are not only more biophysically grounded, but also better suited for capturing the full complexity of large-scale brain dynamics.

The paper is organized as follows. In Section 2 we present the mathematical model. In Section 3 we study the stability of homogeneous states within the homogeneous invariant manifold. In Section 4 we analyze the stability of the homogeneous states with respect to transverse perturbations. In Section 5, we characterize the heterogeneous spatiotemporal patterns that arise when synchronization is lost by means of computations of Lyapunov exponents and frequency spectrum analysis. Finally, we end with a Discussion in Section 6. The Appendix contains details of the linear stability analysis and MSF formalism.

2. Large-scale brain model

We consider a large-scale brain model consisting of a network with $N = 90$ nodes, each representing a distinct brain region defined according to the AAL90 atlas [31] and coupled using structural connectivity data reported in Deco et al. [32]. The number of nodes is thus not arbitrary, but determined by this empirical parcellation. The interactions are defined by a $N \times N$ row-normalized connectivity matrix $\tilde{\boldsymbol{W}} = (\tilde{w}_{jk})$, obtained by averaging the connectomes of 16 human subjects and then applying row normalization so that the entries of each row sum to one (as it is usually employed in large-scale brain models [9,30,39,40]), that is,

$$\sum_{k=1}^{N} \tilde{w}_{jk} = 1. \tag{1}$$

The connection weights $\tilde{w}_{jk}$ are non-negative and indicate the average number of connections from region k to region j, for $j, k \in \{1, \dots, N\}$. The network topology is available at `github.com/pclus/transverse-instabilities`.

We assume each region is capable of generating oscillatory activity through the local interaction of excitatory and inhibitory neuronal populations, a mechanism that has been associated to the emergence of brain rhythms in the gamma frequency range [37]. Therefore, the neural activity of each node is modeled using an adapted form of the next-generation neural mass model presented in Dumont and Gutkin [19] and Reyner-Parra and Huguet [27]. Based on an exact low-dimensional description [17], this model provides the evolution of the mean firing rate r and mean membrane potential v of an excitatory and an inhibitory population of Quadratic Integrate-and-Fire (QIF) neurons coupled through exponentially decaying synaptic activity s. Thus, at each node j, the dynamics are governed by the following 6-dimensional system of differential equations,

$$(E_j)\quad \begin{cases} \tau_E \dot{r}_{E,j} = \frac{\Delta_E}{\pi\tau_E} + 2 r_{E,j} v_{E,j} \\ \tau_E \dot{v}_{E,j} = \bar{\eta}_E + v_{E,j}^2 - (\tau_E \pi r_E)^2 + I_{ext}^E + \tau_E (J_{EE} s_{E,j} - J_{EI} s_{I,j} + I_j) \\ \tau_{s_E} \dot{s}_{E,j} = -s_{E,j} + r_{E,j} \end{cases}$$

$$(I_j)\quad \begin{cases} \tau_I \dot{r}_{I,j} = \frac{\Delta_I}{\pi\tau_I} + 2 r_{I,j} v_{I,j} \\ \tau_I \dot{v}_{I,j} = \bar{\eta}_I + v_{I,j}^2 - (\tau_I \pi r_{I,j})^2 + I_{ext}^I + \tau_I (J_{IE} s_{E,j} - J_{II} s_{I,j} + I_j) \\ \tau_{s_I} \dot{s}_{I,j} = -s_{I,j} + r_{I,j} \end{cases} \tag{2}$$

where $r_{\ell,j}$ and $v_{\ell,j}$, with $\ell \in \{E, I\}$ are the mean firing rate and mean membrane potential of population ℓ in node j, respectively. The variable s_ℓ represents the synaptic current from population ℓ. Parameters τ_ℓ and τ_{s_ℓ} are the membrane and synaptic time constants, respectively. For $p, q \in \{E, I\}$, J_{pq} is the connection strength from population q to population p. At the single neuron description, each unit receives a different input current, which can be either static and drawn from a Cauchy distribution [17] or Cauchy white noise [41,42]. In either case, parameters η_ℓ and Δ_ℓ are, respectively, the center and width of the distribution of such inputs. All variables and parameters of the model are dimensionless, except for the time-related quantities. Since t is measured in milliseconds, so are the time constants τ_ℓ and τ_{s_ℓ}, whereas the firing rates r_ℓ are measured in spikes per millisecond (kHz) [21].

Coupling between nodes is mediated by synaptic projections originating from the excitatory populations, while inhibition acts only locally, as in similar models [15]. In our case, these long-range excitatory inputs target both the excitatory and inhibitory populations of the receiving node. The strength of the synaptic couplings is governed by the

Table 1
Parameters of the coupled next generation neural mass model in Eq. (2). The label "Bif. Param." stands for Bifurcation Parameter.

Parameter	Meaning	Value
$\tau_E, \tau_I, \tau_{s_E}, \tau_{s_I}$	Time constants	8, 8, 1, 5 ms
$\bar{\eta}_E, \bar{\eta}_I$	Baseline constant current for E,I neurons	−5, −5
Δ_E, Δ_I	Population heterogeneity or noise strength	1,1
$J_{EE}, J_{EI}, J_{IE}, J_{II}$	Synaptic strength of connection between populations	5, 13, 13, 5
I^E_{ext}, I^I_{ext}	External current impinging in E/I population	Bif. Param., 0
ε	Coupling strength between nodes	Bif. Param.

normalized structural connectivity matrix $\tilde{\boldsymbol{W}}$. Additionally, the overall influence of these long-range interactions is modulated by a global coupling parameter ε, which scales the entire connectivity matrix. Thus, the excitatory inputs from other nodes to population ℓ of node j are given by

$$I_j = \varepsilon \sum_{k=1}^{N} \tilde{w}_{jk} s_{E,k},$$

where $\tilde{w}_{jk}$ are the synaptic weights obtained from the entries of the row-normalized structural connectivity matrix $\tilde{\boldsymbol{W}}$.

We study the system under the influence of the external input to the excitatory population I^E_{ext} and the coupling strength ε, leaving all the other parameters fixed. The parameters are chosen according to [27] and are provided in Table 1.

The row-normalized connectivity matrix ensures that all units in the network receive the same total input, although distributed differently across nodes. This structure guarantees the existence of an invariant manifold, with identical dynamics for all nodes. We refer to this manifold as the *homogeneous invariant manifold*. We use this manifold as a reference structure to explore how instabilities of homogeneous states can emerge and generate complex spatiotemporal dynamics. To understand such collective behavior, we first study this simplified state of identical node dynamics.

3. Homogeneous invariant manifold

In this section, we derive the equations governing the dynamics on the homogeneous invariant manifold and analyze their solutions and local stability to determine which homogeneous states are stable under uniform perturbations.

Let $\boldsymbol{y}_j = (r_{E,j}, v_{E,j}, s_{E,j}, r_{I,j}, v_{I,j}, s_{I,j})$ denote the variables describing the dynamics of node j. Imposing that $\boldsymbol{y}_j = \boldsymbol{y} := (r_E, v_E, s_E, r_I, v_I, s_I)$ for all $j = 1, \ldots, N$, and using Eq. (1), the incoming input for each brain region in (2) becomes

$$I_j = \varepsilon \sum_{k=1}^{N} \tilde{w}_{jk} s_{E,k} = \varepsilon s_E \sum_{k=1}^{N} \tilde{w}_{jk} = \varepsilon s_E, \tag{3}$$

so it does not depend on the node index j anymore. Replacing expression (3) in the input current I_j of both excitatory and inhibitory populations in (2), the equations describing the dynamics on the homogeneous manifold become

$$\text{(E)} \quad \begin{cases} \tau_E \dot{r}_E = \frac{\Delta_E}{\pi \tau_E} + 2 r_E v_E, \\ \tau_E \dot{v}_E = \bar{\eta}_E + v_E^2 - (\tau_E \pi r_E)^2 + I^E_{ext} + \tau_E [(J_{EE} + \varepsilon) s_E - J_{EI} s_I], \\ \tau_{s_E} \dot{s}_E = -s_E + r_E, \end{cases}$$

$$\text{(I)} \quad \begin{cases} \tau_I \dot{r}_I = \frac{\Delta_I}{\pi \tau_I} + 2 r_I v_I, \\ \tau_I \dot{v}_I = \bar{\eta}_I + v_I^2 - (\tau_I \pi r_I)^2 + I^I_{ext} + \tau_I [(J_{IE} + \varepsilon) s_E - J_{II} s_I], \\ \tau_{s_I} \dot{s}_I = -s_I + r_I. \end{cases} \tag{4}$$

This low-dimensional system captures the dynamics of spatially homogeneous states of the full system (2). Note that due to the row normalization of $\tilde{\boldsymbol{W}}$, the dynamics on the homogeneous manifold is independent of the specific network topology and depends only on the scalar coupling strength parameter ε. Moreover, within the homogeneous manifold, ε has the same effect as varying J_{EE} and J_{IE} simultaneously. However, this global coupling parameter has a different impact on transverse stability, studied in Section 4.

Local stability analysis of Eq. (4) reveals how solutions respond to uniform perturbations, that is, those that affect all nodes in an identical manner, a task we address in the next section. We emphasize that, while homogeneous dynamics are not a realistic brain state, their comprehensive analysis provides the necessary information to uncover the emergence of complex behavior in the full model (Eq. (2)).

3.1. Dynamics on the homogeneous invariant manifold

In this section, we analyze the dynamics of system (4) as external excitatory input I^E_{ext} and coupling strength ε vary. We use the bifurcation analysis software AUTO-07p [43] to identify invariant objects of the homogeneous system (4) and explore their stability within the homogeneous manifold.

Fig. 1A shows the bifurcation diagram of the uncoupled model ($\varepsilon = 0$ in (4)) as I^E_{ext} is varied. For low values of I^E_{ext}, there exists a unique stable state of the system given by an equilibrium point, corresponding to asynchronous activity of the neuronal population described by the neural mass model. This equilibrium loses stability via a supercritical Hopf bifurcation (HB^+_1) at $I^E_{ext} \approx 5$. Therefore, a stable limit cycle emerges and persists until $I^E_{ext} \approx 65$, where it vanishes at another supercritical Hopf bifurcation (HB^+_2) of the equilibrium point, which transitions back to stable. This oscillatory activity corresponds to gamma activity, with frequencies in the range of 27–170 Hz as I^E_{ext} varies (results obtained using AUTO-07p; not shown).

Including coupling $\varepsilon > 0$ in system (4) modifies this bifurcation scenario. In general, the oscillatory region becomes narrower and new invariant objects arise, which leads to richer and more complex behavior. Namely, for $\varepsilon = 12$ (see Fig. 1B), the limit cycle loses stability through a period-doubling bifurcation (PD_1) at $I^E_{ext} \approx 9$. This bifurcation gives rise to a new limit cycle with twice the period of the first periodic orbit. As I^E_{ext} increases further, successive period-doubling bifurcations (PD_2, PD_3, …) occur, forming a period-doubling cascade that may signal the onset of deterministic chaos [44]. In Section 3.2 we provide an in-depth analysis of this situation.

As ε is increased further, there appear regions of bistability, characterized by the simultaneous presence of two stable attractors. Namely, for $\varepsilon = 15$ (see Fig. 1C), we observe the coexistence of two stable limit cycles and one unstable limit cycle, which coalesce at a pair of fold of limit cycle bifurcations (FLC_1 and FLC_2). For $\varepsilon = 26$, we encounter a region of bistability between an equilibrium point and a limit cycle. In this case, the bistability emerges through the second Hopf bifurcation (HB^-_2), which is now subcritical, where the equilibrium point recovers stability and an unstable limit cycle appears and persists until it coalesces with the stable limit cycle at a fold of limit cycles (FLC_2). Also for $\varepsilon = 26$, two saddle-node bifurcations of the already unstable fixed points occur within the oscillatory region (not marked in the diagram).

These dynamics can be more clearly organized in the two-parameter bifurcation diagram shown in Fig. 1E, which allows us to identify the regions of oscillatory states in the parameter space (I^E_{ext}, ε). Fixed points,

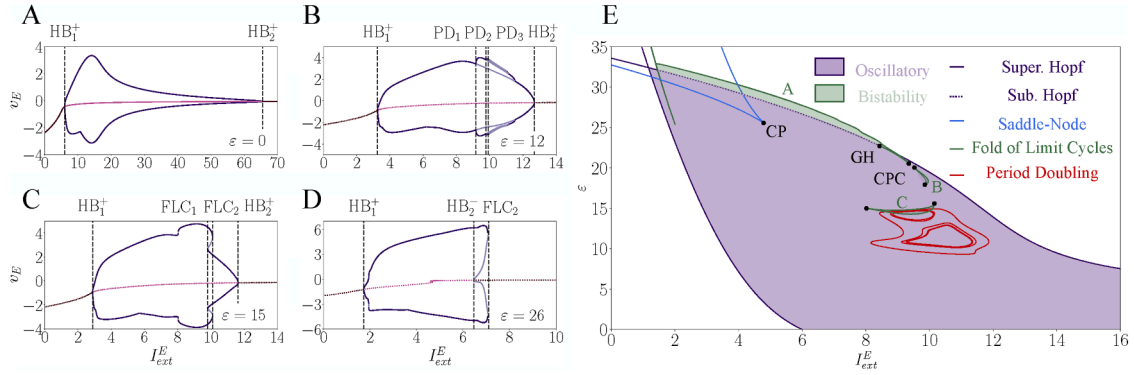

Fig. 1. Bifurcation diagram of the homogeneous system (4). **(A-D)** One-parameter bifurcation diagram of Eq. (4) for varying I^E_{ext} and with fixed **(A)** $\varepsilon = 0$, **(B)** $\varepsilon = 12$, **(C)** $\varepsilon = 15$ and **(D)** $\varepsilon = 26$. Colored dotted curves indicate stable equilibrium points (dark pink), unstable equilibrium point (light pink), extrema of stable limit cycle (dark purple) and extrema of unstable limit cycle (light purple). Dashed vertical lines indicate relevant bifurcation points (see text). **(E)** Two-parameter bifurcation diagram of system (4) for varying I^E_{ext} and ε. Colored curves indicate the different bifurcations: supercritical Hopf (solid purple), subcritical Hopf (dashed purple), saddle-node (blue), fold of limit cycles (green), period doubling (red). The light purple region indicates a single periodic state, while the light green region indicates bistability (see text).

representing asynchronous activity, destabilize through Hopf bifurcations (purple curves), giving rise to collective oscillations, mainly in the gamma range (purple region) that may be stable or unstable depending on parameter values. Solid (resp. dashed) purple curves correspond to supercritical (resp. subcritical) Hopf bifurcations, with the transition occurring at a generalized Hopf (GH) or Bautin codimension-2 bifurcation at $I^E_{ext} \approx 8.48, \varepsilon \approx 22.65$. Moreover, oscillations also vanish or emerge through fold of limit cycles (FLC) bifurcations (green curves), some of them colliding at a cusp of limit cycles (CPC) codimension-2 bifurcations.

Thus, oscillations occur in the purple and green regions enclosed by the Hopf and FLC bifurcations. In the green region A, the system presents bistability between asynchronous and oscillatory activity. There is also a tiny region (intersection of purple and green region A) showing bistability between two different types of oscillations. Indeed, in this region the system presents three limit cycles, two of them stable and one unstable, in addition to the unstable equilibrium point. Within the oscillatory purple region, there appear two islands of bistability (green regions labeled with *B* and *C*) bounded by FLC bifurcations that coalesce at different cusps of limit cycles (indicated with black dots). For ε in the range 10–15, we identified a closed curve of period-doubling bifurcations (red), with further period-doubling bifurcations inside (red curves), suggesting a period-doubling cascade.

For large coupling values ε, two branches of saddle-node bifurcations (blue) appear, enclosing a region of bistability between two fixed points. These curves meet at a cusp point (CP) around $I^E_{ext} \approx 4.82, \varepsilon \approx 25.43$. At higher ε, additional bifurcations arise, leading to new codimension-2 bifurcations. Nonetheless, within the range explored using AUTO-07p, no stable periodic solutions were found beyond the purple and green regions depicted in Fig. 1E.

3.2. Period-doubling cascade and deterministic chaos

The bifurcation diagram shown in Fig. 1E reveals a region of nested closed curves of period-doubling bifurcations, suggesting the presence of deterministic chaos. In this section, we investigate this phenomenon in detail.

We begin by exploring the chaotic region at $\varepsilon = 12$, which intersects the region of period-doubling curves in the two-parameter bifurcation diagram (see Fig. 1B), while varying $I^E_{ext} \in [8.5, 12]$. For each value of I^E_{ext}, we integrate the system for 500 ms after disregarding an initial transient. Fig. 2A shows the sequence of local maxima of the excitatory synapse variable s_E, plotted against I^E_{ext}.

In regions where the system exhibits stable periodic behavior, the diagram shows either one or two branches corresponding to either one or two local maxima per oscillation cycle, respectively. As we increase I^E_{ext}, the system undergoes successive period-doubling bifurcations, each doubling the number of maxima and generating a cascade that leads to deterministic chaos, reflected by the presence of dense, irregular patterns in the diagram [44]. The chaotic dynamics are confined to a bounded interval of the parameter space, beyond which the system returns to periodic behavior. Within the chaotic region, we also observe bands of parameter values for I^E_{ext} in which the system maintains a stable behavior, forming islands of stability.

To quantitatively characterize the chaotic dynamics, Fig. 2B shows the two largest Lyapunov exponents λ of the homogeneous system, computed numerically (see Appendix B). For values of I^E_{ext} corresponding to periodic oscillations, the largest Lyapunov exponent (LLE) is zero while the others remain negative. However, for values of I^E_{ext} that lie in the chaotic region, the LLE becomes positive and at the critical values of I^E_{ext}, where period-doubling bifurcations occur, the second-largest Lyapunov exponent becomes zero.

To identify the extent of the chaotic region of the homogeneous system in the two-parameter space, Fig. 2C shows the LLE over (I^E_{ext}, ε). The white area corresponds to the region of stable periodic oscillations, as it exhibits zero LLE. Instead, the colored areas reveal two regions of positive LLE, which fit within the curves of period-doubling bifurcations detected using AUTO-07p (red curves in Fig. 2C). These correspond to the regions of deterministic chaos in the two parameter space. Additionally, the diagram reveals the shape and location of the islands of stability within the chaotic area.

Instances of these chaotic states are depicted in Fig. 2D and E, which show simulations of the homogeneous system for fixed $\varepsilon = 12$ and $I^E_{ext} = 10$ and $I^E_{ext} = 10.5$, respectively. The upper row of each panel provides the time evolution of the excitatory synaptic variable s_E over 500 ms of a trajectory starting from initial conditions set to zero and discarding an initial transient. The lower row, depicts the same trajectory within the three-dimensional subspace spanned by the variables of the excitatory population (r_E, v_E, s_E). In both cases, the system lies in the chaotic regime, exhibiting aperiodic dynamics in which the trajectory ends up densely filling a finite region of the phase space. Hence, the presence of a strange attractor becomes evident.

4. Transverse instabilities

The different dynamical regimes and stability regions uncovered so far concern only perturbations acting uniformly among all brain regions. However, perturbations that are transverse to the homogeneous invariant manifold may drive the dynamics of the large-scale brain model toward heterogeneous neural activity patterns including traveling or

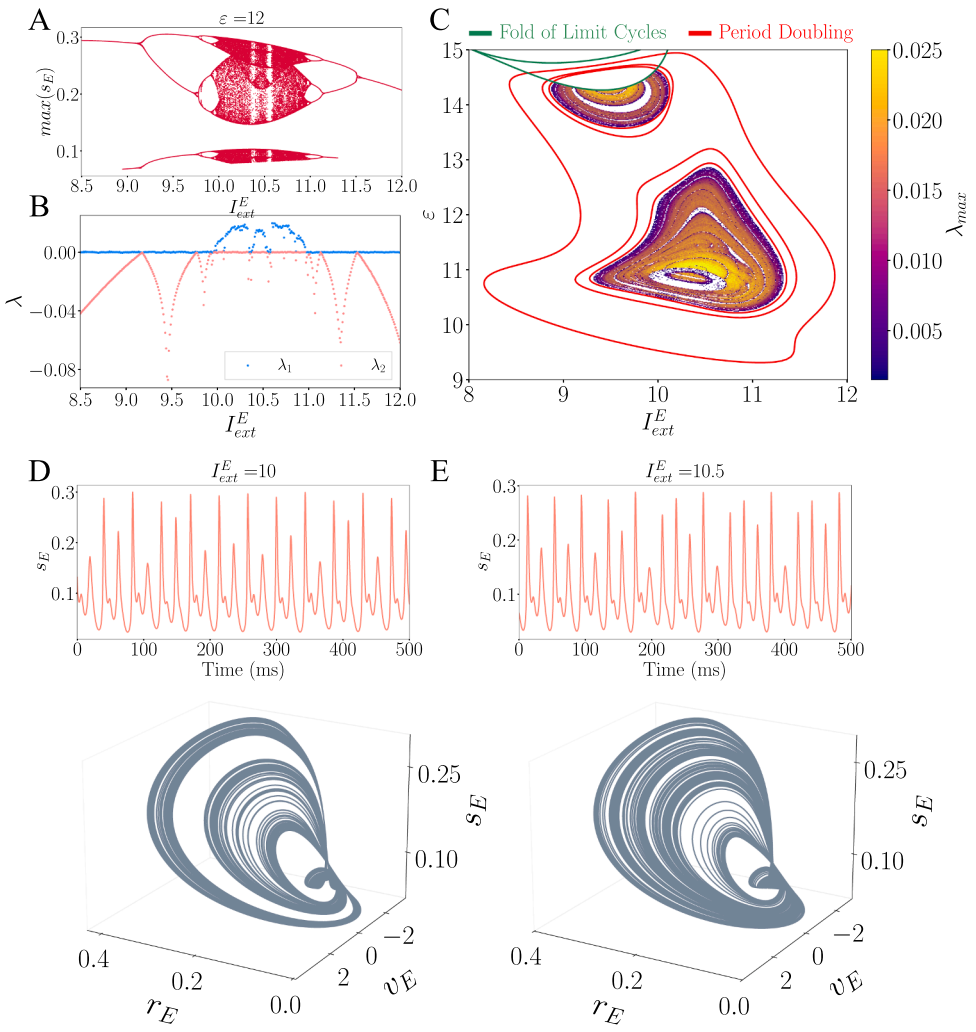

Fig. 2. Analysis of the chaotic region for the homogeneous system (4). **(A)** Local maxima of the time course of s_E variable along a trajectory of system (4) after discarding an initial transient time for fixed $\varepsilon = 12$ and varying $I^E_{ext} \in [8.5, 12]$ with a discretization step $\Delta_{I^E_{ext}} = 0.001$. **(B)** Two largest Lyapunov exponents of system (4) for fixed $\varepsilon = 12$ and varying $I^E_{ext} \in [8.5, 12]$ with a discretization step $\Delta_{I^E_{ext}} = 0.01$. **(C)** Largest Lyapunov exponent of the homogeneous system varying both $\varepsilon \in [8, 12]$ and $I^E_{ext} \in [9, 15]$ with a discretization step $\Delta = 0.01$. The green and red curves represent, respectively, the fold of limit cycles and the period-doubling bifurcation curves computed with AUTO-07p. **(D-E)** Simulated trajectories of the homogeneous system (4) for fixed $\varepsilon = 12$ and $I^E_{ext} = 10$ **(D)** and $I^E_{ext} = 10.5$ **(E)** showing convergence to the attracting solution after discarding an initial transient. The top plots show the time series of the variable s_E for 500 ms. Bottom plots display the trajectory projected onto the 3-dimensional space (r_E, v_E, s_E) for 5000 ms.

chaotic waves. In this section we perform linear stability analysis of the homogeneous fixed points and limit cycles of the full system (2).

To this end, we apply a well-known technique of projecting the perturbation onto a suitable eigenbasis that decouples the high-dimensional stability problem into simpler, lower-dimensional components associated to different spatial modes. For fixed point solutions, this simply corresponds to the analysis of Turing instabilities in networked systems [45], whereas for limit cycles, the analogous procedure is usually known as the Master Stability Function (MSF) formalism [16]. This method has been widely employed to study systems with diffusive coupling, where the eigenbasis corresponds to the diagonalization of the network Laplacian [45–47]. In coupled neural mass models, however, the coupling is via synaptic variables, thus the eigenbasis where to decompose the perturbations corresponds to the diagonalization of $\tilde{\boldsymbol{W}}$ [15] (see Appendix A for full details).

Indeed, diffusion tensor imaging usually provides symmetric connectivities. The row-normalization of a symmetric matrix, $\tilde{\boldsymbol{W}}$, preserves some diagonalization properties of the original matrix; in particular, $\tilde{\boldsymbol{W}}$ is diagonalizable with real eigenvalues [15]. By construction (see Eq. (1)), its largest eigenvalue is $\Lambda_1 = 1$, with associated eigenvector $\Phi^{(1)} = (1, \dots, 1)$. Moreover, due to the row-normalization of $\tilde{\boldsymbol{W}}$ and the *Gershgorin circle theorem* [48], all other eigenvalues Λ_α, with $\alpha = 2, \dots, N$, are confined within the unit disk, i.e., $\Lambda_\alpha \in [-1, 1]$. The eigenvectors of the normalized structural connectivity matrix, $\Phi^{(\alpha)}$, are also referred to as *eigenmodes* in this context, since they define spatial patterns of activity across the network.

Ultimately, the linear stability analysis based on mode decomposition provides the largest exponential growth rate $\mu^{(\alpha)}_{\max}$ of a perturbation acting along each eigenmode $\boldsymbol{\Phi}^{(\alpha)}$ as a function of its associated eigenvalue Λ_α. That is,

$$\mathcal{F}(\Lambda_\alpha) = \mu^{(\alpha)}_{max}. \tag{5}$$

We refer to this function as the dispersion relation. A positive value of $\mu^{(\alpha)}_{\max}$ implies the instability along the αth eigenmode's direction. If $\alpha > 1$, this usually results in the emergence of (spatially) heterogeneous dynamics. On the contrary, if all $\mu^{(\alpha)}_{\max} < 0$ for all $\alpha = 2, \dots, N$, then small heterogeneous perturbations of the homogeneous state will decay exponentially. In Appendix A we provide a detailed derivation of the method.

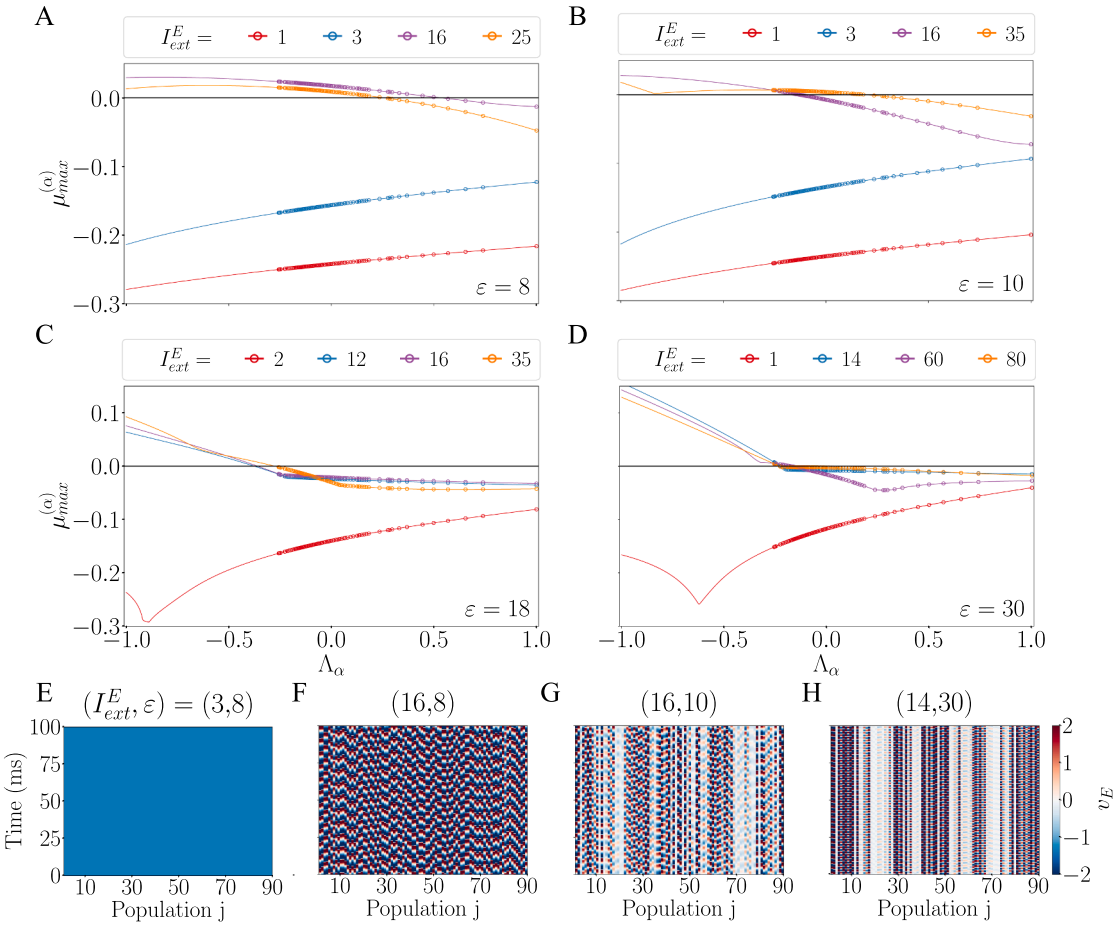

Fig. 3. Transverse instabilities of homogeneous equilibrium points. (**A-D**) Dispersion relation (5) for homogeneous equilibrium points of system (2), showing the dependence of the growth rate $\mu^{(\alpha)}_{\max}$ on the eigenvalues Λ_α of the structural connectivity matrix $\bar{\boldsymbol{W}}$. Parameters are fixed at $\varepsilon = 8$ (**A**), $\varepsilon = 10$ (**B**), $\varepsilon = 18$ (**C**) and $\varepsilon = 30$ (**D**) with different values of I^E_{ext} indicated in each panel. Continuous curves are obtained by considering a continuous range of $\Lambda_\alpha \in [-1, 1]$. (**E-H**) Numerical simulations of the large-scale brain model (2) for different combinations of the parameters (I^E_{ext}, ε), each starting from a homogeneous equilibrium with a small random perturbation. Each plot shows the evolution of the variable v_E (color-coded) for each node $j = 1, \ldots, N$ (x-axis) over 100 ms (y-axis) after discarding an initial transient.

4.1. *Transverse instabilities of homogeneous equilibrium points*

In this section, we study the stability of homogeneous equilibrium points with respect to heterogeneous perturbations by computing the dispersion relation in Eq. (5). In this case, the growth rate $\mu^{(\alpha)}_{\max}$ corresponds to the real part of the dominant eigenvalue of the linearized system around the equilibrium. This quantity thus governs the evolution of perturbations projected onto the eigenmode $\boldsymbol{\Phi}^{(\alpha)}$, for $\alpha = 1, \ldots, N$.

Fig. 3A-D shows the dispersion relation (5) of the stable equilibria of the homogeneous system (4) for selected parameter combinations (I^E_{ext}, ε). Growth rates associated to structural eigenmodes Λ_α are depicted by circles, whereas continuous curves show a visual reference obtained by considering arbitrary values of $\Lambda \in [-1, 1]$. Since the uniform eigenmode, associated to $\Lambda_\alpha = 1$, corresponds to perturbations along the homogeneous manifold, the largest growth rate for perturbations along this direction is negative. The real part of the eigenvalues associated to the remaining eigenmodes may be positive or negative.

For $\varepsilon = 8$ (Fig. 3A) and $\varepsilon = 10$ (Fig. 3B), low values of I^E_{ext} yield negative growth rates across all the eigenmodes, indicating stability of the homogeneous state. However, as I^E_{ext} increases, the dispersion curves are shifted upwards and the growth rates associated to eigenmodes with low structural eigenvalues Λ_α become positive, leading to transverse instabilities of the homogeneous state. As ε increases to $\varepsilon = 18$ (Fig. 3C), the dispersion relation becomes negative for all eigenmodes across the different values of I^E_{ext} explored. Therefore, the homogeneous equilibrium point is transversely stable for all these parameter combinations. Finally, for $\varepsilon = 30$ (Fig. 3D), high values of I^E_{ext} lead to some eigenmodes becoming unstable once again, indicating loss of stability for the equilibrium point.

We remark the effect of the particular network connectivity on determining the stability of the homogeneous state. For instance, in Fig. 3A for $I^E_{ext} = 25$ (orange circles) most directions are unstable, but other network connectivities with higher Λ_α would fall within the negative range of the dispersion relation (indicated by the continuous curve). The opposite happens in Fig. 3C for $I^E_{ext} = 12$, 16, and 35 (blue, purple, and orange circles respectively), where all eigenmodes fall within the negative part of the dispersion relation, but continuous curves show that networks with distinct spectral properties could lead to instability for the same parameter values. Some works exploited this property to modify a network topology to attain a predefined stability profile [49,50].

To evaluate the predictions of the linear stability analysis, we compare them with simulations of the large-scale brain model (Fig. 3E-H) for representative parameter combinations. All simulations start from a homogeneous equilibrium with a small random perturbation, and we show the last 100 ms of a 60 s run. For $\varepsilon = 8$, $I^E_{ext} = 3$ (blue circles in Fig. 3A), the dispersion relation shows that all modes decay (negative growth rate), and the network dynamics decay to the stable homogeneous equilibrium, as seen in Fig. 3E. In contrast, Fig. 3F-H correspond to parameter combinations with a dispersion relation where certain modes have positive growth rates, leading to heterogeneous spatiotemporal

dynamics. It is remarkable that in all cases, destabilization of the homogeneous equilibrium point produces oscillatory patterns with features specific to each parameter set. For example, for $\varepsilon = 10$ (Fig. 3G) and $\varepsilon = 30$ (Fig. 3H), some nodes exhibit oscillations with significantly lower amplitude than others, behavior that is not observed for $\varepsilon = 8$ (see Fig. 3F). In Section 5 we characterize some of these complex states in detail.

4.2. Transverse instabilities of homogeneous periodic orbits

We analyze the stability of homogeneous periodic orbits with respect to heterogeneous perturbations by computing the dispersion relation in Eq. (5), which in the case of periodic orbits is also known as the Master Stability Function (MSF) [16]. In this case, the growth rate $\mu^{(\alpha)}_{\max}$ corresponds to the real part of the largest Floquet exponent of the periodic orbit, which governs the evolution of perturbations applied along the αth eigenmode. In Appendix A.1 we provide details of the numerical computation.

Fig. 4A-D shows the MSF for stable periodic orbits of the homogeneous system (4) for selected parameter combinations (I^E_{ext}, ε). The largest growth rate associated to homogeneous perturbations ($\alpha = 1$) is $\mu^{(1)}_{\max} = 0$, according to Floquet theory. The Floquet exponents associated to the remaining eigenmodes may be positive, negative or zero.

For $\varepsilon = 5$ (Fig. 4A), increasing I^E_{ext} shifts the dispersion curves upward smoothly, preserving their shape. Notably, for larger ε (Fig. 4B-D), the curves change shape more markedly with I^E_{ext}. For instance, at $\varepsilon = 9$ and $I^E_{ext} = 12$ (orange circles in Fig. 4B), the first unstable mode corresponds to $\alpha = 2$, whereas for $I^E_{ext} = 9.5$ (purple circles) the instability occurs first for $\alpha = 5$. At $\varepsilon = 20$ (Fig. 4D), the curves display non-monotonic behavior as I^E_{ext} varies. In addition, the number of eigenmodes that become unstable varies for each parameter combination. Overall, the nontrivial shape of the dispersion relation illustrates the complexity of the bifurcation structure underlying transverse instabilities of the oscillatory states.

The high complexity exhibited by the MSF in our model for different parameter combinations (I^E_{ext}, ε) may influence the types of patterns that arise when the homogeneous state destabilizes. To illustrate so, Fig. 4E-H shows simulations of the large-scale brain model for representative parameter combinations.

For $\varepsilon = 5$ and $I^E_{ext} = 7$ (red circles in Fig. 4A), the dispersion relation shows a negative growth rate for all the structural eigenvalues and the network dynamics decays to the homogeneous periodic state (see Fig. 4E). In contrast, for $I^E_{ext} = 13$ (orange circles in Fig. 4A), the dispersion curve presents some modes with positive Floquet exponents, leading to heterogeneous spatiotemporal dynamics (see Fig. 4F). The patterns emerging from destabilization of the homogeneous oscillatory state vary with parameters. Examples of other spatiotemporal patterns are shown in Fig. 4G-H. For instance, the dynamics for $\varepsilon = 5$ (Fig. 4F) and $\varepsilon = 12$ (Fig. 4G) appears rather heterogeneous, while for $\varepsilon = 20$ (Fig. 4H), it retains some structured organization among some nodes. Section 5 provides an in-depth characterization of these dynamics.

4.3. Bifurcation diagram for transverse instabilities

In this section we thoroughly analyze the regions in the parameter space $(I^E_{ext}, \varepsilon) \in [0, 16] \times [0, 30]$ where we encounter transverse instabilities of the homogeneous states for both equilibrium points and periodic orbits.

For each pair of parameters (I^E_{ext}, ε) we compute the dispersion relation corresponding to the homogeneous solution. Fig. 5A shows, for each pair, the largest growth rate $\hat{\mu}$ among all eigenmodes (excluding the uniform one), that is,

$$\hat{\mu} := \max_{\alpha=2,\dots,N} \{\mu^{(\alpha)}_{max}\}. \tag{6}$$

Two distinct color gradients are used to distinguish whether the underlying solution is a fixed point, $\hat{\mu}_{EQ}$, or a periodic orbit, $\hat{\mu}_{PO}$. For regions with bistability between homogeneous equilibrium and periodic orbits see Figure in Supplementary Data S5. Black curves delimit the regions of transverse instabilities and color curves correspond to bifurcations of the homogeneous system, as in Fig. 1E.

Regarding homogeneous equilibrium points, the region to the left of the Hopf bifurcation HB^+_1 corresponds to a transversely stable equilibrium, as indicated by the strongly negative $\hat{\mu}_{EP}$. In contrast, to the right of the Hopf bifurcation HB_2, the equilibrium point becomes transversely unstable in two parameter regions (warm colors), which are separated by an intermediate band where it is stable (cold colors).

These findings differ from those reported in [15] for the Jansen-Rit model, where all stable equilibrium points in the homogeneous invariant manifold were found to be stable with respect to transverse perturbations.

Concerning homogeneous periodic orbits, the parameter regions where they become transversely unstable show several noteworthy features. In particular, the area with positive $\hat{\mu}_{PO}$ (colored in red in Fig. 5A) displays several distinct lobes characterized by different magnitudes of $\hat{\mu}_{PO}$. For instance, the large lower-right lobe displays smaller values of $\hat{\mu}_{PO}$ compared to the large central lobe, which surrounds the region where the homogeneous system exhibits chaos. Toward the upper left of the oscillatory region, additional lobes appear, alternating in the magnitude of $\hat{\mu}_{PO}$. The more elongated lobes tend to correspond to higher values of $\hat{\mu}_{PO}$, whereas shorter and rounder lobes generally present lower values. Interestingly, in the upper part of the diagram, regions with unstable periodic orbit are consistently surrounded by regions with strongly negative $\hat{\mu}_{PO}$.

This intricate structure of transverse bifurcations is significantly different from the one reported in [15] for the Jansen-Rit model, where only a single, well-defined region with unstable directions was observed.

Fig. 5B shows the number of unstable directions (positive values in the dispersion relation) within the regions with transverse instabilities. For equilibrium points, we observe a high number of unstable directions (up to 89) within the lower unstable region, in contrast to the few (less than 10) unstable modes of the upper region. For oscillations, the lower lobe exhibits few unstable directions, less than 10. In contrast, the central lobe surrounding the chaotic region of the homogeneous state, shows the highest number of unstable directions, reaching up to 89 in the central and lower-right area. As for the upper lobes, the elongated ones display a higher number of unstable directions, around 30–60, while the shorter ones seem to present less unstable directions.

Finally, in Fig. 5C, we investigate the mechanisms underlying the shape of the regions with transverse instabilities. We highlight (in orange) the regions where the second eigenmode ($\alpha = 2$) becomes unstable. This reveals that, in the region with equilibrium points, the instabilities are driven by modes associated with lower values of Λ_α. In contrast, within the oscillatory region, the second mode is the first to destabilize over a large portion of the unstable region. For instance, it completely fills the lower lobe, indicating that here the bifurcation curve is determined by the destabilization of the second eigenmode. However, some parts of the bifurcation curve remain uncovered, thus destabilization occurs through lower values of Λ_α (see Figure in Supplementary Data S6). Again, this behavior highly contrasts with the findings of [15], where transverse instabilities always arose from the destabilization of the second eigenmode ($\alpha = 2$).

5. Heterogeneous spatiotemporal patterns in the large-scale brain model

The analysis in the previous sections identified parameter regions where synchrony breaks down, but it did not characterize the dynamics that follow. In this section, we explore the complex spatiotemporal patterns that emerge beyond the loss of stability of homogeneous solutions. To this end, we adopt two complementary approaches. First, we compute the Lyapunov exponents of system (2) to distinguish chaotic dynamics, particularly high-dimensional chaos, from regular solutions.

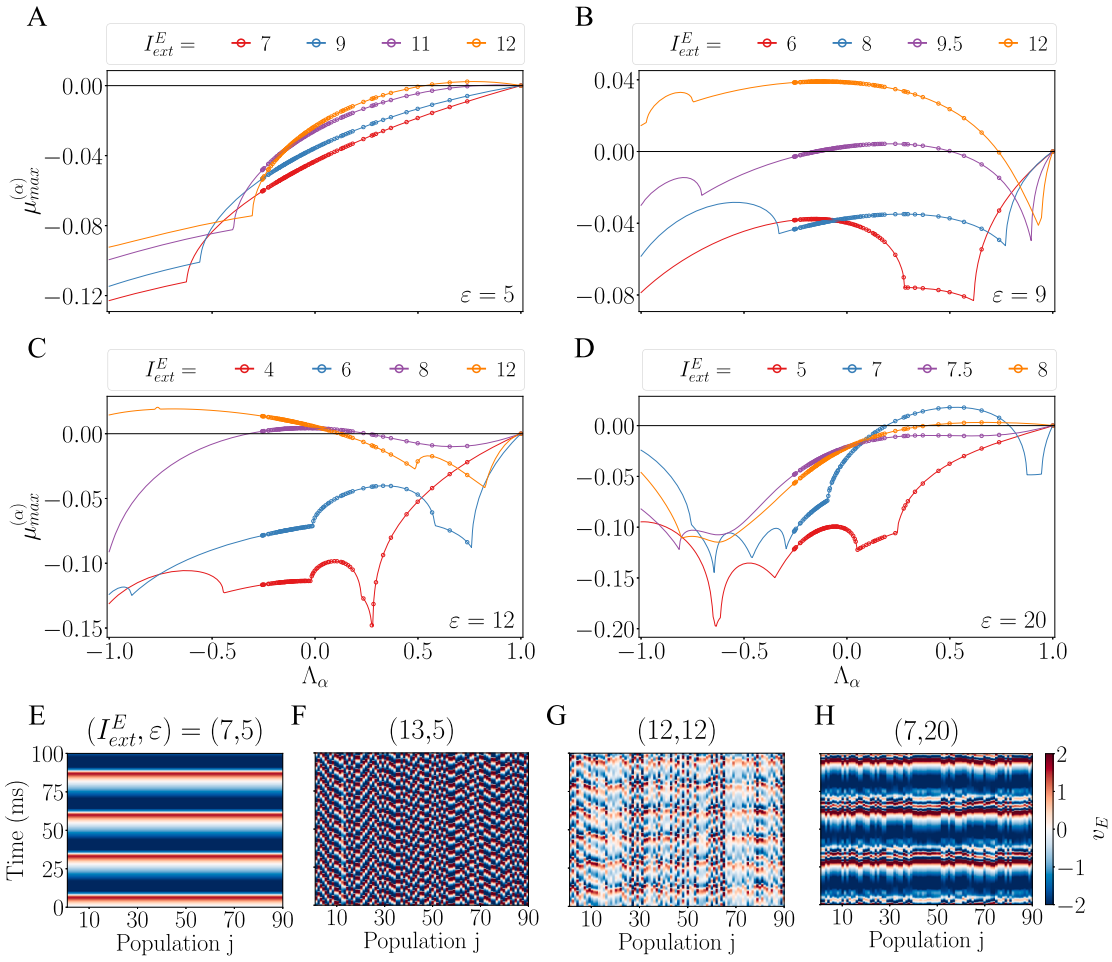

Fig. 4. Transverse instabilities of homogeneous periodic solutions. (**A-D**) Dispersion relation, known as Master Stability Function, for homogeneous periodic orbits of system (2), showing the dependence of the real part of the largest Floquet exponent $\mu^{(\alpha)}_{\max}$ on the structural connectivity eigenvalues Λ_α. Parameters are fixed at $\varepsilon = 5$ (**A**), $\varepsilon = 9$ (**B**), $\varepsilon = 12$ (**C**) and $\varepsilon = 20$ (**D**) with different values of I^E_{ext} indicated in each panel. Continuous curves are obtained by considering a continuous range of $\Lambda_\alpha \in [-1, 1]$. (**E-H**) Numerical simulations of the large-scale brain model (2) for different combinations of parameters (I^E_{ext}, ε), each starting from a point on a homogeneous periodic orbit with a small random perturbation. Each plot shows the evolution of the variable v_E (color-coded) for each node $j = 1, \ldots, N$ (x-axis) over 100 ms (y-axis) after discarding an initial transient.

Then, we perform a Fourier spectral analysis to examine the frequency content of the emergent patterns. This allows us to better characterize whether the system exhibits coherent oscillations or broadband chaotic activity. Indeed, the emergence of high-dimensional chaos aligns with recent studies that highlight the role of turbulent, complex dynamics as an indicator of healthy brain function [5].

5.1. Lyapunov exponents analysis

When the homogeneous state destabilizes, the system can exhibit a rich variety of spatiotemporal patterns. Lyapunov exponents (LE) quantify the growth rates of infinitesimal perturbations of a system's attractor, thus providing a rigorous tool to analyze the nature of these states. We compute the largest 90 Lyapunov exponents $\lambda_1 \geq \ldots \geq \lambda_{90}$ of system (2) using the Julia package ChaosTools (see Appendix B for details). By examining the Largest Lyapunov exponent (LLE), λ_1, we can characterize the dynamics as chaotic ($\lambda_1 > 0$), periodic or quasiperiodic ($\lambda_1 = 0$), or stationary ($\lambda_1 < 0$).

In the case of chaotic dynamics, additional exponents provide valuable information regarding the state's complexity. In particular, we use them to compute the Kaplan-Yorke dimension [51,52], which provides an estimation of the fractal dimension of a strange attractor by measuring how much *volume* in state space is actively being stretched and filled out by the dynamics. This measure is computed as,

$$D_{KY} = j + \frac{\sum_{i=1}^{j} \lambda_i}{|\lambda_{j+1}|}, \tag{7}$$

where j is the largest integer such that

$$\sum_{i=1}^{j} \lambda_i \geq 0 \qquad \text{and} \qquad \sum_{i=1}^{j+1} \lambda_i < 0.$$

Note that if $\lambda_i < 0$ for all i, then $D_{KY} = 0$, indicating contraction in all directions and convergence of the dynamics to a fixed point.

Fig. 6A-C displays the first six Lyapunov exponents (out of the 90 computed) of system (2) for representative values of the coupling strength ε and varying I^E_{ext}. We observe the onset of oscillatory activity, when the largest Lyapunov exponent passes from being negative to being zero, and the onset of chaotic dynamics, when it becomes positive. Notably, for $\varepsilon = 5$, $\varepsilon = 9$, and $\varepsilon = 12$ (Fig. 6A-B-C, respectively), the onset of chaotic dynamics coincides closely with the emergence of transverse instabilities of periodic orbits studied in Sections 4.2 and 4.3. This can be observed by comparing with a horizontal cut at the corresponding ε in Fig. 5. Remarkably, for $\varepsilon = 9$ (Fig. 6B), the largest Lyapunov exponent remains positive at high values of I^E_{ext}, where we have detected transverse instabilities of the equilibrium points (see Fig. 5A). For $\varepsilon = 20$

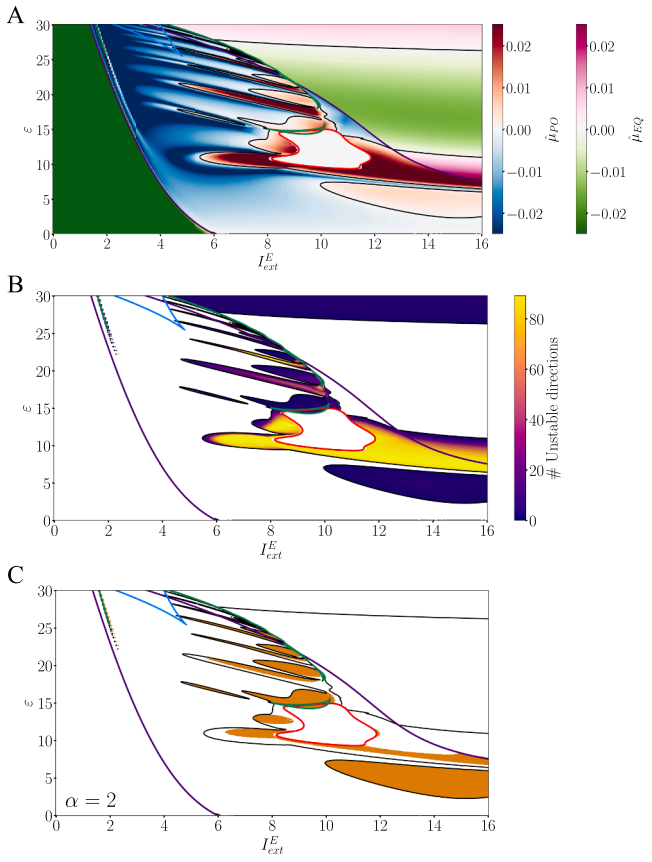

Fig. 5. Bifurcation diagram of transverse instabilities. **(A)** Largest growth rate, $\hat{\mu}$, obtained from the dispersion relation (5) according to formula in Eq. (6), with values for equilibrium points ($\hat{\mu}_{EQ}$) and periodic orbits ($\hat{\mu}_{PO}$) shown using different color gradients. **(B)** Number of unstable directions from the dispersion relation (5). **(C)** Regions (in orange) where the second eigenmode, Λ_2, destabilizes. In all panels, bifurcation curves of the homogeneous system are overlaid using the same color code as in Fig. 1E.

(Fig. 6D), the LLE remains zero over the majority of the transverse instability region, indicating that the destabilization of the homogeneous state gives rise to heterogeneous periodic dynamics, in this case, a traveling wave.

To better identify the features of the chaotic attractor, Fig. 6E displays the Kaplan-Yorke dimension of the system's attractor. High dimensional chaotic dynamics arise at $\varepsilon = 5$, 9, and 12, with attractors with dimension almost 80 in some cases. For $\varepsilon = 9$ and 12, this complexity can be traced back to the high number of unstable directions of the homogeneous state (see Fig. 5B). Nonetheless, for $\varepsilon = 5$ the emergence of high-dimensional dynamics may be less expected, as the underlying homogeneous state contains less than 10 unstable directions (see Fig. 5B). In Supplementary Data S7, we provide a quantitative comparison between the number of unstable transverse directions of the homogeneous state and the resulting Kaplan-Yorke dimension, D_{KY}. The figure reveals a clear positive correlation between these quantities for $\varepsilon = 5, 9$, and 12, where high-dimensional chaos emerges.

Overall, these results show the ubiquity of high-dimensional chaos emerging from transverse instabilities in the parameter space, highlighting thus the dynamical complexity of the brain model.

5.2. Frequency analysis

To further characterize the heterogeneous oscillatory patterns arising from transverse instabilities of homogeneous solutions, we analyze their frequency spectrum. Our goal is to relate the dominant frequency components to the unstable eigenvalues or Floquet exponents of the corresponding homogeneous solutions. To this end, we analyze representative parameter combinations for which homogeneous equilibria or periodic orbits lose stability via different bifurcation mechanisms.

To interpret these spectral features, we recall that when an equilibrium point destabilizes via a supercritical Hopf bifurcation (a pair of complex eigenvalues crosses the imaginary axis) a limit cycle emerges whose frequency near the bifurcation can be approximated by the imaginary part of the corresponding eigenvalues according to the formula

$$f_\mu = \frac{\mathrm{Im}(\mu)}{2\pi}\ (\mathrm{kHz}). \tag{8}$$

Similarly, when a periodic orbit loses stability due to a pair of complex-conjugate Floquet exponents crossing the imaginary axis, a torus (Neimark-Sacker) bifurcation generically occurs [53], leading to quasiperiodic dynamics (provided there are no resonances) characterized by the frequency of the unstable periodic orbit and that associated to the imaginary part of the critical Floquet exponents, as described by Eq. (8). As system parameters vary further, the invariant torus may break down, leading to chaotic dynamics (via the so-called torus breakdown route to chaos [54]). If the Floquet exponents are complex but the corresponding Floquet multipliers are negative real, a flip (period-doubling) bifurcation occurs, potentially initiating a cascade towards chaos.

We simulate the large-scale brain model (2) for 60 s from initial conditions near the unstable homogeneous state, adding a small random heterogeneous perturbation. For each signal, we compute the frequency spectrum of the excitatory membrane potential v_E at each node and report the average spectrum across nodes (with standard deviation) in Figs. 7 and 8. We also show time series of the mean excitatory membrane potential

$$\bar{v}_E(t) = \frac{1}{N}\sum_{j=1}^{N} v_{E,j}(t).$$

To interpret the observed spectral features, we relate them to the linear stability properties of the corresponding homogeneous solutions, examining the number and type (real or complex) of unstable eigenvalues or Floquet exponents and, when complex, computing the associated frequencies using (8). The examples below illustrate how this information helps explain the frequency content of the resulting spatiotemporal dynamics, particularly near the bifurcation where the homogeneous state loses stability.

We first consider homogeneous equilibria (Fig. 7). For $(I^E_{ext}, \varepsilon) = (16, 8)$, the homogeneous solution has 86 complex eigenvalues with positive real part and similar imaginary parts, yielding high-dimensional chaos (Fig. 7A; see also Movie in Supplementary Data S1). The time series of the emerging solution reveals dynamics occurring on at least two different timescales: fast oscillations modulated by a slower, irregular envelope (Fig. 7A, top). The imaginary parts of the destabilizing eigenvalues match the fast frequency peaks in the power spectrum (gray lines in Fig. 7A, bottom), while power at very low frequencies reflects the slow modulation.

In contrast, for $(I^E_{ext}, \varepsilon) = (14, 30)$, the homogeneous equilibrium has only six unstable complex eigenvalues with similar imaginary parts. Here the dynamics converge to a periodic orbit (Fig. 7B; see also Movie in Supplementary Data S2) with a single dominant fast oscillatory component. Its fundamental frequency is well captured by the imaginary parts of the destabilizing eigenvalues (Fig. 7B, bottom).

Next, we explore patterns emerging from the destabilization of homogeneous periodic orbits (Fig. 8). For $(I^E_{ext}, \varepsilon) = (13, 5)$, the homogeneous solution has 5 real positive Floquet exponents. Despite the low number of unstable directions, the resulting dynamics are chaotic (see Fig. 8A top and Movie in Supplementary Data S3), similar to Fig. 7A. The power spectrum (Fig. 8A bottom) exhibits broad peaks around the fast frequency, captured by the frequency of the unstable periodic solution (red vertical line), along with significant power at low frequencies.

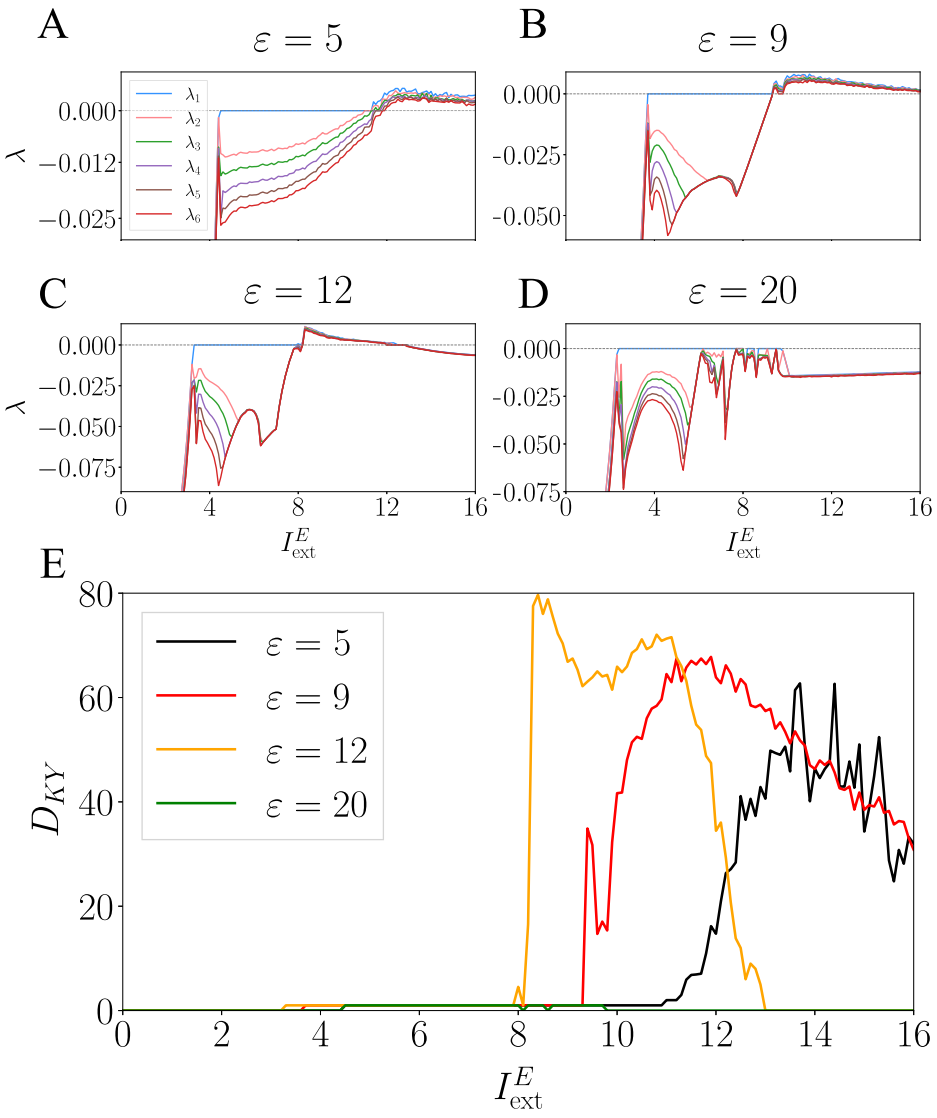

Fig. 6. Lyapunov exponents of the large-scale brain model. (**A-D**) First six largest Lyapunov exponents of system (2) as a function of $I^E_{ext} \in [0, 16]$ with discretization step $\Delta_{I^E_{ext}} = 0.1$ and fixed $\varepsilon = 5$ (**A**), $\varepsilon = 9$ (**B**), $\varepsilon = 12$ (**C**) and $\varepsilon = 20$ (**D**). For each parameter combination, the 90 largest Lyapunov exponents were computed starting from initial conditions near the homogeneous state with a small random perturbation. (**E**) Kaplan-Yorke dimension of the chaotic attractor, computed according to Eq. (7).

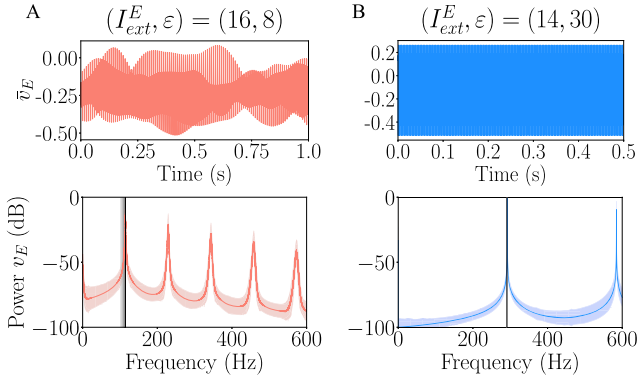

Fig. 7. Frequency spectrum of patterns emerging from homogeneous unstable equilibria. For the parameter combinations (**A**) $(I^E_{ext}, \varepsilon) = (16, 8)$ and (**B**) $(I^E_{ext}, \varepsilon) = (14, 30)$, top panels display time series of the mean excitatory membrane potential $\bar{v}_E(t)$ computed across nodes for solutions of the large-scale brain model (2) starting near the unstable homogeneous equilibrium. Each simulation was run for 60 s with a time step of 0.01, discarding the first 10 s to remove transients. Bottom panels display the average frequency spectrum across all nodes (solid curve) with the corresponding standard deviation (shaded area). Vertical gray lines correspond to the frequencies obtained from the imaginary part of the eigenvalues $\mu^{(\alpha)}_{\max}$ with positive real part. The sampling frequency is $f_s = 10^5$ samples per second and yielding a frequency resolution of $\Delta f = 0.02$ Hz.

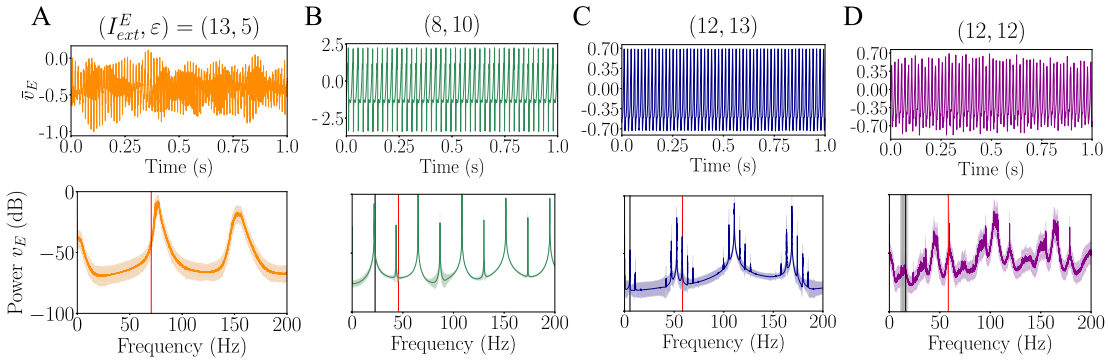

Fig. 8. Frequency spectrum of patterns emerging from homogeneous unstable periodic orbits. Analogous to Fig. 7, for the parameter combinations **(A)** $(I^E_{ext}, \varepsilon) = (13, 5)$, **(B)** $(I^E_{ext}, \varepsilon) = (8, 10)$, **(C)** $(I^E_{ext}, \varepsilon) = (12, 13)$ and **(D)** $(I^E_{ext}, \varepsilon) = (12, 12)$, (top) time series of the mean excitatory membrane potential $\bar{v}_E(t)$ computed across nodes for solutions of the large-scale brain model (2) starting near the unstable homogeneous periodic orbit. Each simulation was run for 60 s with a time step of 0.01, discarding the first 10 s to remove transients. Bottom panels display the average frequency spectrum across all nodes (solid curve) with the corresponding standard deviation (shaded area). The vertical red line corresponds to frequency of the homogeneous unstable periodic orbit, while the vertical gray lines correspond to the frequencies obtained from the imaginary part of the complex Floquet exponents $\mu^{(\alpha)}_{\max}$ with positive real part. The sampling frequency is $f_s = 10^5$ samples per second and yielding a frequency resolution of $\Delta f = 0.02$ Hz.

For $(I^E_{ext}, \varepsilon) = (8, 10)$ the system exhibits a regular periodic orbit (Fig. 8B top; see also Movie in Supplementary Data S4). The homogeneous solution has 85 unstable directions, with complex Floquet exponents associated to a period-doubling bifurcation. The fundamental frequency of the solution is approximately half that of the unstable periodic orbit (red vertical line in Fig. 8B bottom).

For $(I^E_{ext}, \varepsilon) = (12, 13)$ the system exhibits a fast oscillation modulated by a slower rhythm (Fig. 8C, top; see also Figure in Supplementary Data S8). The homogeneous periodic solution has four complex Floquet exponents with positive real part and distinct imaginary parts. The power spectrum (Fig. 8C, bottom) exhibits sidebands around the fast (gamma) frequency (which closely matches that of the unstable periodic orbit) with slow modulation in the theta range (4–8 Hz), captured by the imaginary parts of the Floquet exponents. This behavior represents an intriguing emergent pattern: phase-amplitude coupling, a type of cross-frequency interaction commonly observed in brain recordings and linked to cognitive functions such as memory and information transmission (see Discussion for details).

For $(I^E_{ext}, \varepsilon) = (12, 12)$, the spectrum (Fig. 8D) is similar to that in Fig. 8C, but with broader peaks, indicating chaotic dynamics (see also Figure in Supplementary Data S9). Interestingly, in the latter case, the unstable periodic orbit has 71 unstable directions. In both cases, power is higher at twice the fundamental frequency, due to secondary peaks in voltage traces (see Fig. S8C and S9C).

6. Discussion

In this work, we have investigated how complex spatiotemporal patterns emerge in a large-scale, data-driven brain model whose network architecture is determined by an empirically derived 90-region connectome. Our study extends the analysis of [15], which mostly focused on Jansen-Rit neural mass models for the dynamics in the nodes, primarily associated with slower rhythms. In contrast, the present framework incorporates a next-generation neural mass model tuned to generate gamma-band oscillations via the PING mechanism [19,27].

This modification of the local dynamics substantially enriches the global behavior of the system. For instance, the homogeneous manifold displays a wider dynamical landscape than in [15], including bistability, period-doubling cascades, and widespread chaotic regimes. Moreover, we identify multiple instability regions emerging from both equilibria and periodic solutions. This also contrasts with [15], where transverse instabilities arise only from periodic orbits within a single region of parameter space.

Beyond the homogeneous manifold, the destabilization of homogeneous states leads to a broad spectrum of spatiotemporal behaviors in the full network, including high-dimensional chaos and periodic traveling waves. Detailed numerical analysis of these regimes show two key results: First, the prevalence of high-dimensional chaos, confirmed by Lyapunov exponents, suggests that irregular dynamics may be a robust feature of these models. Second, the imaginary parts of the homogeneous states' critical growth rates (Jacobian eigenvalues or Floquet exponents) often reflect the dominant spectral components of the heterogeneous patterns. This connection provides a mechanistic interpretation for the different emerging regimes consistent with Hopf, Neimark-Sacker, or period-doubling bifurcations.

A particularly relevant class of solutions corresponds to nodes showing gamma oscillations with amplitude modulated by slower theta (4–8 Hz) or alpha (8–12 Hz) components (see Fig. 8C and D). This form of rhythmic activity is commonly observed in the brain and is a type of cross-frequency coupling known as phase-amplitude coupling [1]. Specifically, theta-gamma coupling is believed to play a central role in coordinating neural computation and information processing, particularly within the hippocampus and neocortex [38,55–57]. Remarkably, in our model, this slow modulation emerges spontaneously from interactions among nodes that individually exhibit only intrinsic gamma dynamics, without the need to introduce a separate slower oscillator, as is typically required in other models [25,58]. These findings highlight the crucial role of anatomical connectivity in shaping rhythmic brain patterns and motivate further exploration of its mechanistic implications.

Overall, this work reveals the impact of the local dynamics on the ultimate global behavior of the system, showing that next-generation neural mass models offer a complex and rich bifurcation landscape. A potential reason for this increased variety of dynamics compared to other models are the additional time scales in NG-NMM. Indeed, in classical models, the dynamics depend only on synaptic transmission, with the firing rate given by a static sigmoid on the input current. Instead, NG-NMMs incorporate two additional variables, r and v, on top of synaptic kinetics. These effectively capture the spiking dynamics, thus generalizing the heuristic setting and incorporating one more time scale for each neural population considered [21,59–62].

Recent studies have also employed large-scale brain models in which the nodes are governed by a neural mass model similar to the NG-NMM used here [15,28–30]. In Forrester et al. [30], a model with additional gap junctions and synapses is shown to reproduce FC patterns observed in MEG and fMRI, although the analysis is limited to linear stability of homogeneous equilibria near Hopf bifurcations. In Perl et al. [29], the

emphasis is on the effects of structural and functional heterogeneities, but without a detailed analytical investigation of the underlying dynamics. In Gerster et al. [28], the node model is reduced to a single excitatory population, and the analysis focuses on transitions between low- and high-activity states associated with seizure-like events, thereby restricting attention to equilibrium points rather than periodic orbits. In contrast, our work extends the analytical treatment to include homogeneous periodic orbits and provides a characterization of emergent complex spatiotemporal patterns through Lyapunov exponents and frequency spectra. Finally, although [15] mostly focuses on classical NMMs, it also briefly reports on transverse instabilities emerging from limit cycles in a model composed of excitation-inhibition pairs of NG-NMMs to illustrate the generality of the methods. The present work employs a different system for the single node dynamics, which includes synaptic kinetics, and offers a much more detailed and curated analysis of the stability properties of emerging dynamical regimes of the brain model.

Most large-scale brain models are designed to reproduce empirical functional and structural connectivity (FC and SC) data [30,63]. To this end, they typically incorporate additional modeling features such as noise [63,64], axonal delays [64,65], or node heterogeneity [66]. While these elements improve biological realism, they also increase model complexity and hinder systematic mathematical analysis, making it difficult to identify the mechanisms responsible for the observed dynamical patterns.

In the present work, we adopt a complementary perspective by incorporating SC extracted from data while placing the main emphasis on mathematical analysis. This choice requires at least two key assumptions: identical neural mass dynamics across brain regions and a row-normalized network topology. These simplifications, widely used in the field [9,30,39,40] neglect intrinsic cellular and dynamical heterogeneity. A systematic assessment of how these assumptions influence the underlying bifurcation diagram constitutes an important direction for future work. For instance, in Clusella et al. [15], it was shown that simulations of the unnormalized model agree qualitatively with the bifurcation diagram of the row-normalized model, and that the resulting heterogeneities are proportional to each node's degree.

Remarkably, despite its simplicity, our analytically treatable modeling approach is intrinsically capable of generating complex spatiotemporal dynamics and identifies transverse instabilities as a generic route for the emergence of such behavior. An important next step will therefore be to assess the ability of the resulting spatiotemporal dynamics to reproduce experimentally observed functional patterns. Another natural direction for future work concerns modifications of the structural connectivity matrix and their impact on the regions of transverse instability. This includes comparing these regions when using connectomic data from healthy subjects and from individuals with psychiatric or neurological conditions.

At the same time, some modeling features that increase biological realism could be incorporated without entirely sacrificing analytical tractability. In particular, including distance-dependent axonal delays would lead to a system of delay differential equations and could give rise to additional delay-induced bifurcations [19], further enriching the range of attainable patterns.

A similar strategy can be applied to the representation of long-range excitatory interactions. Most long-range projections in the brain, including corticocortical and thalamocortical pathways, are predominantly excitatory (glutamatergic) and typically target both excitatory neurons and local GABAergic interneurons in their destination regions [67,68]. This dual targeting plays a critical role in maintaining excitatory/inhibitory (E/I) balance and in shaping overall network activity. In the present model, this organization is captured by allowing projections from excitatory populations to reach both excitatory and inhibitory neurons across target areas. Future work could explore how these long-range connectivity patterns shape the underlying dynamical landscape by introducing distinct coupling strengths for excitatory and inhibitory populations (ε_E and ε_I).

In summary, this work shows that analytically tractable large-scale brain models equipped with next-generation neural mass dynamics can generate a wide range of complex spatiotemporal behaviors through transverse instabilities. By linking local bifurcations on the homogeneous manifold to emergent heterogeneous dynamics, our results provide a mechanistic perspective on the origins of high-dimensional chaos and structured rhythmic activity in connectome-based models.

CRediT authorship contribution statement

Rosa Maria Delicado-Moll: Writing – original draft, Visualization, Software, Investigation, Formal analysis, Data curation; **Gemma Huguet:** Writing – review & editing, Writing – original draft, Visualization, Validation, Supervision, Methodology, Investigation, Conceptualization; **Pau Clusella:** Writing – review & editing, Writing – original draft, Visualization, Validation, Supervision, Software, Methodology, Investigation, Formal analysis, Conceptualization.

Data availability

All data and code used in this study are openly available. Access links to the repositories are provided in the article.

Declaration of competing interest

The authors declare that they have no known competing financial interests or personal relationships that could have appeared to influence the work reported in this paper.

Acknowledgments

Work produced with the support of the grants PID2024-155942NB-I00 and PID-2021-122954NB-I00 funded by MCIN/AEI/10.13039/501100011033 and "ERDF: A way of making Europe", the Maria de Maeztu Award for Centers and Units of Excellence in R&D (CEX2020-001084-M). We also acknowledge the use of the UPC Dynamical Systems group's cluster for research computing https://dynamicalsystems.upc.edu/en/computing/.

Supplementary material

Supplementary material associated with this article can be found in the online version at 10.1016/j.physd.2026.135232.

Appendix A. Linear stability analysis

Consider $y^{(0)} = (y_0^{(0)}, \dots, y_5^{(0)})^T$ a solution of the homogeneous system (4) (either an equilibrium point or a periodic orbit) and

$$\boldsymbol{y}^{(0)} = (\underbrace{y_0^{(0)}, \dots, y_5^{(0)}}_{\text{Node 1}}, \dots, \underbrace{y_0^{(0)}, \dots, y_5^{(0)}}_{\text{Node } N})^T, \tag{A.1}$$

a homogeneous solution of the network model (2). Consider an arbitrary small perturbation of $\boldsymbol{y}^{(0)}$,

$$\boldsymbol{\delta y} = (\underbrace{\delta y_{0,1}, \dots, \delta y_{5,1}}_{\text{Node 1}}, \dots, \underbrace{\delta y_{0,N}, \dots, \delta y_{5,N}}_{\text{Node } N})^T, \tag{A.2}$$

where each component $\delta y_{k,j}$ represents the perturbation acting on the kth variable of the jth node. Then, the linear evolution of the perturbation is given by

$$\frac{d}{dt}\boldsymbol{\delta y}(t) = \boldsymbol{J}(\boldsymbol{y}^{(0)})\boldsymbol{\delta y}(t), \tag{A.3}$$

where $\boldsymbol{J}$ is the full $6N \times 6N$ Jacobian matrix of the network system (2) evaluated at $\boldsymbol{y}^{(0)}$. The Jacobian matrix of the network can be decomposed in a term containing the Jacobian of the uncoupled system for each node and a coupling term as follows

$$\boldsymbol{J}(\boldsymbol{y}^{(0)}) = \boldsymbol{I}_N \otimes J(y^{(0)}) + \varepsilon \tilde{\boldsymbol{W}} \otimes K, \tag{A.4}$$

where $\otimes$ represents the *Kronecker product*, J is the 6×6 Jacobian matrix of system (4) with $\varepsilon = 0$, $K = (k_{ij})$ is a 6×6 matrix whose entries are given by

$$k_{ij} = \begin{cases} 1 & \text{if } i \in \{2,5\}, j = 3 \\ 0 & \text{otherwise,} \end{cases} \tag{A.5}$$

$\boldsymbol{I}_N$ is the $N\times N$ identity matrix, and $\tilde{\boldsymbol{W}}$ is the normalized structural connectivity matrix.

In order to simplify the analysis, we follow a well-established method which decouples Eq. (A.3) into N first-order variational equations (each of dimension 6), one for each eigenmode of the normalized connectivity matrix $\tilde{\boldsymbol{W}}$ [16,45]. To apply the method, the perturbation vector $\boldsymbol{\delta y}$ is expressed in the eigenbasis of $\tilde{\boldsymbol{W}}$. Let $\boldsymbol{\Phi}^{(\alpha)} = (\phi_1^{(\alpha)}, \dots, \phi_N^{(\alpha)})^T$ be a normalized eigenvector with associated eigenvalue Λ_α for $\alpha = 1, \dots, N$, then the set of eigenvectors

$$\boldsymbol{P} = \left(\boldsymbol{\Phi}^{(1)} | \dots | \boldsymbol{\Phi}^{(j)} | \dots | \boldsymbol{\Phi}^{(N)}\right),$$

constitute a basis of the vector space $\mathbb{R}^N$, and we have $\tilde{\boldsymbol{W}}\boldsymbol{P} = \boldsymbol{P}\boldsymbol{D}$ with $\boldsymbol{D} = \mathrm{diag}(\Lambda_1, \dots, \Lambda_N)$. Let $u^{(\alpha)}(t) = (u_0^{(\alpha)}(t), \dots, u_5^{(\alpha)}(t))^T$ for $\alpha = 1, \dots, N$ be the coordinates of $\boldsymbol{\delta y}(t)$ in this new basis. Then the perturbation of variable k at node j writes as

$$\delta y_{k,j}(t) = \sum_{\alpha=1}^{N} u_k^{(\alpha)}(t)\phi_j^{(\alpha)},$$

and the global perturbation vector for all the network becomes

$$\boldsymbol{\delta y}(t) = \sum_{\alpha=1}^{N} \boldsymbol{\Phi}^{(\alpha)} \otimes u^{(\alpha)}(t). \tag{A.6}$$

Expressing system (A.3) in this basis yields. First,

$$\frac{d}{dt}\boldsymbol{\delta y}(t) = \frac{d}{dt}\left(\sum_{\alpha=1}^{N} \boldsymbol{\Phi}^{(\alpha)} \otimes u^{(\alpha)}(t)\right) = \sum_{\alpha=1}^{N} \boldsymbol{\Phi}^{(\alpha)} \otimes \frac{d}{dt}\left(u^{(\alpha)}(t)\right).$$

On the other hand, using (A.4), we get

$$\frac{d}{dt}\boldsymbol{\delta y}(t) = \boldsymbol{J}(\boldsymbol{y}^{(0)})\boldsymbol{\delta y}(t) = (\boldsymbol{I}_N \otimes J(y^{(0)}) + \varepsilon\tilde{\boldsymbol{W}} \otimes K)\left(\sum_{\alpha=1}^{N} \boldsymbol{\Phi}^{(\alpha)} \otimes u^{(\alpha)}(t)\right) =$$

$$= \sum_{\alpha=1}^{N} (\boldsymbol{I}_N \boldsymbol{\Phi}^{(\alpha)}) \otimes (J(y^{(0)})u^{(\alpha)}(t)) + \varepsilon \sum_{\alpha=1}^{N} (\tilde{\boldsymbol{W}}\boldsymbol{\Phi}^{(\alpha)}) \otimes (Ku^{(\alpha)}(t)) =$$

$$= \sum_{\alpha=1}^{N} \boldsymbol{\Phi}^{(\alpha)} \otimes (J(y^{(0)})u^{(\alpha)}(t)) + \varepsilon \sum_{\alpha=1}^{N} (\Lambda_\alpha \boldsymbol{\Phi}^{(\alpha)}) \otimes (Ku^{(\alpha)}(t)) =$$

$$= \sum_{\alpha=1}^{N} \boldsymbol{\Phi}^{(\alpha)} \otimes (J(y^{(0)})u^{(\alpha)}(t)) + \varepsilon \sum_{\alpha=1}^{N} \boldsymbol{\Phi}^{(\alpha)} \otimes (\Lambda_\alpha K u^{(\alpha)}(t)) =$$

$$= \sum_{\alpha=1}^{N} \boldsymbol{\Phi^{(\alpha)}} \otimes (J(y^{(0)}) + \varepsilon\Lambda_\alpha K)u^{(\alpha)}(t).$$

Imposing the equality of both equations, and using the linear independence of the eigenvectors of the basis, $\boldsymbol{\Phi}^{(\alpha)}$ for $\alpha = 1, \dots, N$, we obtain N variational equations

$$\frac{d}{dt}u^{(\alpha)}(t) = \mathcal{J}(y^{(0)}, \Lambda_\alpha)\, u^{(\alpha)}(t), \quad \text{for } \alpha = 1, \dots, N, \tag{A.7}$$

where

$$\mathcal{J}(y^{(0)}, \Lambda_\alpha) := J(y^{(0)}) + \varepsilon\Lambda_\alpha K,$$

is a family of 6×6 Jacobians that depend on the homogeneous state of the system $y^{(0)}$ and on the eigenvalues of the structural connectivity matrix Λ_α. If we consider $y^{(0)}$ to be a fixed point, then we can analyze the stability of the homogeneous solution by studying the eigenvalues of the Jacobian $\mathcal{J}$. If we consider $y^{(0)} = y^{(0)}(t)$ to be a periodic solution, then $\mathcal{J}$ is a periodic matrix and Floquet theory applies.

Our procedure consists of computing the largest real part of the eigenvalues of $\mathcal{J}$ (for equilibrium points) or Floquet exponent (for periodic orbits) for each $\alpha = 1, \dots, N$, that we denote $\mu_{\max}^{(\alpha)}$ thus obtaining a dispersion relation that characterizes the stability of each mode. Therefore we obtain the largest growth rate $\mu_{\max}^{(\alpha)}$ of a perturbation acting along each eigenmode $\boldsymbol{\Phi}^{(\alpha)}$ as a function of its associated eigenvalue Λ_α (Eq. (5) in the main text). For the case of periodic orbits, this relation is known as Master Stability Function (MSF) [16].

A.1. Numerical computation of the MSF for periodic orbits

In the case of periodic orbits we compute the MSF as follows: First, we compute an initial condition lying on a periodic orbit $y_0(t)$, as well as its period T. The variational Eq. (A.7), consist of a 6-dimensional system of linear periodic differential equations. Thus, we compute a fundamental matrix by solving the initial value problem

$$\frac{d}{dt}U_\alpha(t) = \mathcal{J}(y_0(t), \Lambda_\alpha)\, U_\alpha(t), \quad U_\alpha(0) = I_{6\times 6},$$

associated to each eigenvalue Λ_α, for $\alpha = 1, \dots, N$. Then, we compute the 6 eigenvalues of the monodromy matrix $U_\alpha(T)$, obtaining the Floquet multipliers $\{\sigma_i^{(\alpha)}\}_{i=1}^6$, and take the largest real part of the corresponding Floquet exponents as

$$\mu_{max}^{(\alpha)} = \max_{i=1,\dots,6}\left\{\mathrm{Re}\left(\frac{1}{T}\log\sigma_i^{(\alpha)}\right)\right\},$$

where log is the complex logarithm. Repeating this procedure for every $\alpha = 1, \dots, N$, provides us with the Master Stability Function (5), each α capturing the largest growth rate along each eigenmode.

Appendix B. Numerical methods

Equations for the homogeneous system (4) were integrated numerically in Python [69] using the Runge-Kutta method of order 4-5 (RK45), while the equations of the large-scale brain model (2) were integrated numerically in Julia [70], which offers improved computational performance, using the Runge-Kutta method of order 4 (RK4) with an absolute tolerance ranging between order 10^{-8} and 10^{-9}. All the simulations of the large-scale brain model presented in Sections 4 and 5 have been run for 50 s after discarding an initial transient time of 10 s. Since these sections deal with heterogeneous perturbations (transverse instabilities) of the homogeneous solution, the initial conditions have been set by selecting an homogeneous state and adding an independent random perturbation to each variable normally distributed with 0 mean and 0.01 standard deviation.

Bifurcation diagrams of the homogeneous system (4) were obtained using the bifurcation analysis software AUTO-07p [43].

Lyapunov exponents were computed using the Julia package ChaosTools [71,72]. Simulations for Lyapunov exponents of the full network consisted of 4 s of computation after discarding a 1 s transient, with a time step of $dt = 0.1$ ms. Time windows between consecutive QR-decomposition calls were set to 10 ms. Lyapunov exponents were considered zero if their absolute value fell below the tolerance 10^{-3}.

All codes used in this work have been released and are publicly available at https://github.com/RosaDelic/LargeScaleBrainModelAnalysis.git.

References

[1] G. Buzsáki, Rhythms of the Brain, Oxford university press, 2006.
[2] L. Muller, F. Chavane, J. Reynolds, T.J. Sejnowski, Cortical travelling waves: mechanisms and computational principles, Nat. Rev. Neurosci. 19 (5) (2018) 255–268. https://doi.org/10.1038/nrn.2018.20
[3] H. Zhang, A.J. Watrous, A. Patel, J. Jacobs, Theta and alpha oscillations are traveling waves in the human neocortex, Neuron 98 (6) (2018) 1269–1281.e4. https://doi.org/10.1016/j.neuron.2018.05.019
[4] M. Halgren, I. Ulbert, H. Bastuji, D. Fabó, L. Erőss, M. Rey, O. Devinsky, W.K. Doyle, R. Mak-McCully, E. Halgren, L. Wittner, P. Chauvel, G. Heit, E. Eskandar, A. Mandell, S.S. Cash, The generation and propagation of the human alpha rhythm, Proc. Natl. Acad. Sci. 116 (47) (2019) 23772–23782. https://doi.org/10.1073/pnas.1913092116

[5] G. Deco, M.L. Kringelbach, Turbulent-like dynamics in the human brain, Cell Rep. 33 (10) (2020) 108471. https://doi.org/10.1016/j.celrep.2020.108471

[6] H.R. Wilson, J.D. Cowan, Excitatory and inhibitory interactions in localized populations of model neurons, Biophys. J. 12 (1) (1972) 1–24. https://doi.org/10.1016/S0006-3495(72)86068-5

[7] B.H. Jansen, V.G. Rit, Electroencephalogram and visual evoked potential generation in a mathematical model of coupled cortical columns, Biol. Cybern. 73 (4) (1995) 357–366. https://doi.org/10.1007/BF00199471

[8] F. Wendling, P. Benquet, F. Bartolomei, V. Jirsa, Computational models of epileptiform activity, J. Neurosci. Methods 260 (2016) 233-251. https://doi.org/10.1016/j.jneumeth.2015.03.027

[9] T. Kunze, A. Hunold, J. Haueisen, V. Jirsa, A. Spiegler, Transcranial direct current stimulation changes resting state functional connectivity: a large-scale brain network modeling study, Neuroimage 140 (2016) 174–187. https://doi.org/10.1016/j.neuroimage.2016.02.015

[10] J. Cabral, H.M. Fernandes, T.J. Van Hartevelt, A.C. James, M.L. Kringelbach, G. Deco, Structural connectivity in schizophrenia and its impact on the dynamics of spontaneous functional networks, Chaos Interdiscip. J. Nonlinear Sci. 23 (4) (2013) 046111. https://doi.org/10.1063/1.4851117

[11] L. Stefanovski, P. Triebkorn, A. Spiegler, M.-A. Diaz-Cortes, A. Solodkin, V. Jirsa, A.R. McIntosh, P. Ritter, for the Alzheimer's Disease Neuroimaging Initiative, Linking molecular pathways and large-scale computational modeling to assess candidate disease mechanisms and pharmacodynamics in alzheimer's disease, Front. Comput. Neurosci. 13 (2019) 54. https://doi.org/10.3389/fncom.2019.00054

[12] V.M. Saenger, J. Kahan, T. Foltynie, K. Friston, T.Z. Aziz, A.L. Green, T.J. van Hartevelt, J. Cabral, A.B.A. Stevner, H.M. Fernandes, et al., Uncovering the underlying mechanisms and whole-brain dynamics of deep brain stimulation for Parkinson's disease, Sci. Rep. 7 (1) (2017) 9882.

[13] M.P. Richardson, Large scale brain models of epilepsy: dynamics meets connectomics, J. Neurol. Neurosurg. Psychiatry 83 (12) (2012) 1238–1248. https://doi.org/10.1136/jnnp-2011-301944

[14] S. Olmi, S. Petkoski, M. Guye, F. Bartolomei, V. Jirsa, Controlling seizure propagation in large-scale brain networks, PLoS Comput. Biol. 15 (2) (2019) e1006805. https://doi.org/10.1371/journal.pcbi.1006805

[15] P. Clusella, G. Deco, M.L. Kringelbach, G. Ruffini, J. Garcia-Ojalvo, Complex spatiotemporal oscillations emerge from transverse instabilities in large-scale brain networks, PLoS Comput. Biol. 19 (4) (2023) e1010781.

[16] L.M. Pecora, T.L. Carroll, Master stability functions for synchronized coupled systems, Phys. Rev. Lett. 80 (10) (1998) 2109–2112. Publisher: American Physical Society, https://doi.org/10.1103/PhysRevLett.80.2109

[17] E. Montbrió, D. Pazó, A. Roxin, Macroscopic description for networks of spiking neurons, Phys. Rev. X 5 (2) (2015) 021028.

[18] S. Coombes, A. Byrne, Next generation neural mass models, Springer (2019) 1–16. https://doi.org/10.1007/978-3-319-71048-8_1

[19] G. Dumont, B. Gutkin, Macroscopic phase resetting-curves determine oscillatory coherence and signal transfer in inter-coupled neural circuits, PLoS Comput. Biol. 15 (5) (2019) e1007019.

[20] C. Bick, M. Goodfellow, C.R. Laing, E.A. Martens, Understanding the dynamics of biological and neural oscillator networks through exact mean-field reductions: a review, J. Math. Neurosci. 10 (1) (2020) 9. https://doi.org/10.1186/s13408-020-00086-9

[21] P. Clusella, E. Köksal-Ersöz, J. Garcia-Ojalvo, G. Ruffini, Comparison between an exact and a heuristic neural mass model with second-order synapses, Biol. Cybern. (2022). https://doi.org/10.1007/s00422-022-00952-7

[22] A. Ferrara, D. Angulo-Garcia, A. Torcini, S. Olmi, Population spiking and bursting in next-generation neural masses with spike-frequency adaptation, Phys. Rev. E 107 (2023) 024311. https://doi.org/10.1103/PhysRevE.107.024311

[23] S. Coombes, Next generation neural population models, Front. Appl. Math. Stat. 9 (2023). https://doi.org/10.3389/fams.2023.1128224

[24] V. Pyragas, K. Pyragas, Effect of Cauchy noise on a network of quadratic integrate-and-fire neurons with non-Cauchy heterogeneities, Phys. Lett. A 480 (2023) 128972. https://doi.org/10.1016/j.physleta.2023.128972

[25] M. Segneri, H. Bi, S. Olmi, A. Torcini, Theta-nested gamma oscillations in next generation neural mass models, Front. Comput. Neurosci. 14 (2020). https://doi.org/10.3389/fncom.2020.00047

[26] H. Taher, A. Torcini, S. Olmi, Exact neural mass model for synaptic-Based working memory, PLoS Comput. Biol. 16 (12) (2020) e1008533. https://doi.org/10.1371/journal.pcbi.1008533

[27] D. Reyner-Parra, G. Huguet, Phase-locking patterns underlying effective communication in exact firing rate models of neural networks, PLoS Comput. Biol. 18 (5) (2022) e1009342.

[28] M. Gerster, H. Taher, A. Škoch, J. Hlinka, M. Guye, F. Bartolomei, V. Jirsa, A. Zakharova, S. Olmi, Patient-specific network connectivity combined with a next generation neural mass model to test clinical hypothesis of seizure propagation, Front. Syst. Neurosci. 15 (2021). https://doi.org/10.3389/fnsys.2021.675272

[29] Y.S. Perl, G. Zamora-Lopez, E. Montbrió, M. Monge-Asensio, J. Vohryzek, S. Fittipaldi, C.G. Campo, S. Moguilner, A. Ibañez, E. Tagliazucchi, B.T.T. Yeo, M.L. Kringelbach, G. Deco, The impact of regional heterogeneity in whole-brain dynamics in the presence of oscillations, Netw. Neurosci. 7 (2) (2023) 632-660. https://doi.org/10.1162/netn_a_00299

[30] M. Forrester, S. Petros, O. Cattell, Y.M. Lai, R.D. O'Dea, S. Sotiropoulos, S. Coombes, Whole brain functional connectivity: insights from next generation neural mass modelling incorporating electrical synapses, PLoS Comput. Biol. 20 (12) (2024) e1012647. https://doi.org/10.1371/journal.pcbi.1012647

[31] N. Tzourio-Mazoyer, B. Landeau, D. Papathanassiou, F. Crivello, O. Etard, N. Delcroix, B. Mazoyer, M. Joliot, Automated anatomical labeling of activations in SPM using a macroscopic anatomical parcellation of the MNI MRI single-subject brain, Neuroimage 15 (1) (2002) 273–289. https://doi.org/10.1006/nimg.2001.0978

[32] G. Deco, J. Cabral, M.W. Woolrich, A.B.A. Stevner, T.J. Van Hartevelt, M.L. Kringelbach, Single or multiple frequency generators in on-going brain activity: a mechanistic whole-brain model of empirical MEG data, Neuroimage 152 (2017) 538–550.

[33] M.A. Whittington, R.D. Traub, J.G.R. Jefferys, Synchronized oscillations in interneuron networks driven by metabotropic glutamate receptor activation, Nature 373 (6515) (1995) 612-615. https://doi.org/10.1038/373612a0

[34] M.A. Whittington, R.D. Traub, N. Kopell, B. Ermentrout, E.H. Buhl, Inhibition-based rhythms: experimental and mathematical observations on network dynamics, Int. J. Psychophysiol. 38 (3) (2000) 315-336. https://doi.org/10.1016/s0167-8760(00)00173-2

[35] C. Börgers, S. Epstein, N.J. Kopell, Gamma oscillations mediate stimulus competition and attentional selection in a cortical network model, Proc. Natl. Acad. Sci. 105 (46) (2008) 18023-18028. https://doi.org/10.1073/pnas.0809511105

[36] M. Bartos, I. Vida, P. Jonas, Synaptic mechanisms of synchronized gamma oscillations in inhibitory interneuron networks, Nat. Rev. Neurosci. 8 (1) (2007) 45–56. https://doi.org/10.1038/nrn2044

[37] G. Buzsáki, X.-J. Wang, Mechanisms of gamma oscillations, Annu. Rev. Neurosci. 35 (1) (2012) 203-225. https://doi.org/10.1146/annurev-neuro-062111-150444

[38] J.E. Lisman, O. Jensen, The theta-gamma neural code, Neuron 77 (6) (2013) 1002-1016. https://doi.org/10.1016/j.neuron.2013.03.007

[39] J. Hlinka, S. Coombes, Using computational models to relate structural and functional brain connectivity, Eur. J. Neurosci. 36 (2) (2012) 2137-2145. https://doi.org/10.1111/j.1460-9568.2012.08081.x

[40] J.A. Roberts, L.L. Gollo, R.G. Abeysuriya, G. Roberts, P.B. Mitchell, M.W. Woolrich, M. Breakspear, Metastable brain waves, Nat. Commun. 10 (1) (2019) 1056. https://doi.org/10.1038/s41467-019-08999-0

[41] P. Clusella, E. Montbrió, Exact low-dimensional description for fast neural oscillations with low firing rates, Phys. Rev. E 109 (1) (2024) 014229. https://doi.org/10.1103/PhysRevE.109.014229

[42] B. Pietras, R. Cestnik, A. Pikovsky, et al., Exact finite-dimensional description for networks of globally coupled spiking neurons, Phys. Rev. E 107 (2) (2023) 024315. https://doi.org/10.1103/PhysRevE.107.024315

[43] E.J. Doedel, A.R. Champneys, F. Dercole, T.F. Fairgrieve, Y.A. Kuznetsov, B. Oldeman, R.C. Paffenroth, B. Sandstede, X.J. Wang, C.H. Zhang, AUTO-07P: continuation and bifurcation software for ordinary differential equations, Concordia University, Montreal, QC (2007). https://depts.washington.edu/bdecon/workshop2012/auto-tutorial/documentation/auto07p%20manual.pdf

[44] S.H. Strogatz, Nonlinear Dynamics and Chaos: With Applications to Physics, Biology, Chemistry, and Engineering, Chapman and Hall/CRC, 2024.

[45] H. Nakao, A.S. Mikhailov, Turing patterns in network-organized activator-inhibitor systems, Nat. Phys. 6 (7) (2010) 544–550. https://doi.org/10.1038/nphys1651

[46] H. Nakao, Complex ginzburg-landau equation on networks and its non-uniform dynamics, Eur. Phys. J. Spec. Top. 223 (12) (2014) 2411–2421. https://doi.org/10.1140/epjst/e2014-02220-1

[47] M. Asllani, J.D. Challenger, F.S. Pavone, L. Sacconi, D. Fanelli, The theory of pattern formation on directed networks, Nat. Commun. 5 (1) (2014) 4517. https://doi.org/10.1038/ncomms5517

[48] J.H. Wilkinson, The Algebraic Eigenvalue Problem, Monographs on numerical analysis, Clarendon Press, 1967.

[49] G. Cencetti, F. Bagnoli, G. Battistelli, L. Chisci, F. Di Patti, D. Fanelli, Topological stabilization for synchronized dynamics on networks, Eur. Phys. J. B 90 (1) (2017) 9. https://doi.org/10.1140/epjb/e2016-70465-y

[50] G. Cencetti, P. Clusella, D. Fanelli, Pattern invariance for reaction-diffusion systems on complex networks, Sci. Rep. 8 (1) (2018) 16226. https://doi.org/10.1038/s41598-018-34372-0

[51] J.L. Kaplan, J.A. Yorke, Chaotic behavior of multidimensional difference equations, in: H.-O. Peitgen, H.-O. Walther (Eds.), Functional Differential Equations and Approximation of Fixed Points, Springer Berlin Heidelberg, Berlin, Heidelberg, 1979, pp. 204–227.

[52] A. Pikovsky, A. Politi, Lyapunov Exponents: A Tool to Explore Complex Dynamics, Cambridge University Press, 2016.

[53] Y.A. Kuznetsov, Elements of Applied Bifurcation Theory, Springer International Publishing, 2023. https://doi.org/10.1007/978-3-031-22007-4

[54] D. Ruelle, F. Takens, On the nature of turbulence, Commun. Math. Phys. 20 (3) (1971) 167-192. https://doi.org/10.1007/bf01646553

[55] G. Buzsáki, The Hippocampo-Neocortical dialogue, Cereb. Cortex 6 (2) (1996) 81-92. https://doi.org/10.1093/cercor/6.2.81

[56] R. Scheffer-Teixeira, A.B.L. Tort, Theta-Gamma Cross-Frequency Analyses (Hippocampus), Springer New York, 2018, p. 1-15. https://doi.org/10.1007/978-1-4614-7320-6_100658-1

[57] J. Jackson, F.K. Skinner, Hippocampus, Theta, Gamma, and Cross-Frequency Coupling, Springer New York, 2018, p. 1-11. https://doi.org/10.1007/978-1-4614-7320-6_30-2

[58] A. Ceni, S. Olmi, A. Torcini, D. Angulo-Garcia, Cross frequency coupling in next generation inhibitory neural mass models, Chaos Interdiscip. J. Nonlinear Sci. 30 (5) (2020) 053121. https://doi.org/10.1063/1.5125216

[59] F. Devalle, A. Roxin, E. Montbrió, Firing rate equations require a spike synchrony mechanism to correctly describe fast oscillations in inhibitory networks, PLoS Comput. Biol. 13 (12) (2017) e1005881. https://doi.org/10.1371/journal.pcbi.1005881

[60] F. Castaldo, R. de Palma Aristides, P. Clusella, J. Garcia-Ojalvo, G. Ruffini, Rosetta stone of neural mass models, 2025, https://arxiv.org/abs/2512.10982.

[61] R. Barrio, J.A. Jover-Galtier, A. Mayora-Cebollero, C. Mayora-Cebollero, S. Serrano, Synaptic dependence of dynamic regimes when coupling neural populations, Phys. Rev. E 109 (2024) 014301. https://doi.org/10.1103/PhysRevE.109.014301

[62] A. Mayora-Cebollero, R. Barrio, L. Li, C. Mayora-Cebollero, L. Pérez, Dynamics of coupled neural populations: the role of synaptic dynamics, Chaos Interdiscip. J. Nonlinear Sci. 35 (6) (2025). https://doi.org/10.1063/5.0219780

[63] G. Deco, M.L. Kringelbach, V.K. Jirsa, P. Ritter, The dynamics of resting fluctuations in the brain: metastability and its dynamical cortical core, Sci. Rep. 7 (1) (2017). https://doi.org/10.1038/s41598-017-03073-5

[64] G. Deco, V. Jirsa, A.R. McIntosh, O. Sporns, R. Kötter, Key role of coupling, delay, and noise in resting brain fluctuations, Proc. Natl. Acad. Sci. 106 (25) (2009) 10302-10307. https://doi.org/10.1073/pnas.0901831106

[65] S. Petkoski, V.K. Jirsa, Transmission time delays organize the brain network synchronization, Phil. Trans. R. Soc. A Math. Phys. Eng. Sci. 377 (2153) (2019) 20180132. https://doi.org/10.1098/rsta.2018.0132

[66] A. Ponce-Alvarez, G. Deco, P. Hagmann, G.L. Romani, D. Mantini, M. Corbetta, Resting-state temporal synchronization networks emerge from connectivity topology and heterogeneity, PLoS Comput. Biol. 11 (2) (2015) e1004100. https://doi.org/10.1371/journal.pcbi.1004100

[67] R.J. Douglas, K.A.C. Martin, Neuronal Circuits of the Neocortex, Annu. Rev. Neurosci. 27 (1) (2004) 419-451. https://doi.org/10.1146/annurev.neuro.27.070203.144152

[68] J.S. Isaacson, M. Scanziani, How inhibition shapes cortical activity, Neuron 72 (2) (2011) 231-243. https://doi.org/10.1016/j.neuron.2011.09.027

[69] P.S. Foundation, Python Language Reference, version 3.11, 2023, (https://www.python.org/).

[70] J. Bezanson, A. Edelman, S. Karpinski, V.B. Shah, Julia: a fresh approach to numerical computing, SIAM Rev. 59 (1) (2017) 65–98.

[71] G. Datseris, DynamicalSystems. JL: a Julia software library for chaos and nonlinear dynamics, J. Open Source Software 3 (23) (2018) 598.

[72] G. Datseris, E. Fosong, Y. Liu, A. Braun, A. Wagemakers, K.L. Rossi, A. Singhvi, A. Hill, J. Isensee, I. Kottlarz, T. Arakaki, A.S. Rao, A. Rusu, J. TagBot, spaette, ChaosTools, 2023, https://doi.org/10.5281/zenodo.10026773.